Mapping dark matter and finding filaments: calibration of lensing analysis techniques on simulated data

Sut-Ieng Tam [ID],[1][*] Richard Massey [ID],[1] Mathilde Jauzac [ID][1,2,3] and Andrew Robertson [ID][1]

[1]*Institute for Computational Cosmology, Durham University, South Road, Durham DH1 3LE, UK*
[2]*Centre for Extragalactic Astronomy, Durham University, South Road, Durham DH1 3LE, UK*
[3]*Astrophysics and Cosmology Research Unit, School of Mathematical Sciences, University of KwaZulu-Natal, Durban 4041, South Africa*

ABSTRACT

We quantify the performance of mass mapping techniques on mock imaging and gravitational lensing data of galaxy clusters. The optimum method depends upon the scientific goal. We assess measurements of clusters' radial density profiles, departures from sphericity, and their filamentary attachment to the cosmic web. We find that mass maps produced by direct (KS93) inversion of shear measurements are unbiased, and that their noise can be suppressed via filtering with MRLENS. Forward-fitting techniques, such as LENSTOOL, suppress noise further, but at a cost of biased ellipticity in the cluster core and overestimation of mass at large radii. Interestingly, current searches for filaments are noise-limited by the intrinsic shapes of weakly lensed galaxies, rather than by the projection of line-of-sight structures. Therefore, space-based or balloon-based imaging surveys that resolve a high density of lensed galaxies could soon detect one or two filaments around most clusters.

Key words: gravitational lensing: weak – techniques: image processing – galaxies: clusters: general – large-scale structure of Universe.

1 INTRODUCTION

The Lambda cold dark matter (ΛCDM) standard model of cosmology suggests that structures in the Universe formed hierarchically, via mergers of small overdensities in the early Universe into larger and larger objects (White & Rees 1978; Springel et al. 2005; Schaye et al. 2015). Thirteen billion years after the big bang, the largest objects are currently clusters of hundreds or thousands of galaxies. Because their growth has spanned the entire age of the Universe, and has depended upon the density of building material and its collapse under gravity, versus its disruption by supernovae, active galactic nuclei, and dark energy, measurements of the precise number and properties of clusters are a highly sensitive test of the standard cosmological model (e.g. Bahcall & Cen 1993; Bahcall & Bode 2003; Ho, Bahcall & Bode 2006; Rozo et al. 2010; Weinberg et al. 2015; Jauzac et al. 2016; Schwinn et al. 2017; Mao et al. 2018; Fluri et al. 2019).

Gravitational lensing is particularly efficient at investigating clusters. The dense concentration of mass in a foreground galaxy cluster deflects light rays emitted by unrelated galaxies far in the background. Since adjacent light rays are almost coherently deflected, the shapes of those distant galaxies appear distorted, and typically stretched in such a way that their long axes make circular patterns around the cluster. Crucially, the deflection of light rays depends only upon the total projected mass distribution. Measurements of gravitational lensing are therefore uniquely sensitive to the distribution of invisible-but-dominant dark matter, and unbiased by the nature and dynamical state of ordinary matter (e.g. Massey, Kitching & Richard 2010; Kneib & Natarajan 2011; Hoekstra 2013; Kilbinger 2015; Treu & Ellis 2015; Bartelmann & Maturi 2017).

Ground-based observations of gravitational lensing by galaxy clusters have been successfully used to measure clusters' average or bulk properties, such as mass (e.g. Umetsu et al. 2014; von der Linden et al. 2014; Okabe & Smith 2016; Medezinski et al. 2018; Sereno et al. 2017; Schrabback et al. 2018; Herbonnet et al. 2019; McClintock et al. 2019; Miyatake et al. 2019; Rehmann et al. 2019; Umetsu et al. 2020) and ellipticity (e.g. Evans & Bridle 2009; Oguri et al. 2010; Clampitt & Jain 2016; van Uitert et al. 2017; Chiu et al. 2018; Shin et al. 2018; Umetsu et al. 2018). The CLASH survey (Cluster Lensing and Supernova Survey with Hubble; Postman et al. 2012) measured the mass and concentration of 25 clusters, by combining wide-field Subaru imaging with *Hubble Space Telescope* (*HST*) imaging of the cluster cores (Merten et al. 2015). However, ground-based observations have yielded only marginally significant detections of filaments (e.g. Kaiser et al. 1998; Gray et al. 2002; Gavazzi et al. 2004; Clowe et al. 2006; Dietrich et al. 2012; Martinet et al. 2016), whose dark matter density is too low (and the filaments too narrow to resolve).

Space-based imaging reveals the shapes of more background galaxies, and increases the S/N of lensing measurements in multiple resolution elements across an individual cluster. Thus, the shape

[*] E-mail: sut-ieng.tam@durham.ac.uk

and morphology of individual mass distributions can be precisely *mapped*, without the need to average out features over a population of clusters. Space-based lensing reconstructions have resolved substructure near cluster cores (e.g. Merten et al. 2011; Natarajan et al. 2017); bimodality even in relatively distant clusters like the 'Bullet Cluster' (Bradac et al. 2006) or 'El Gordo' (Jee et al. 2014); and filaments in Abell 901/902 (Heymans et al. 2008) and MACSJ 0717+3745 (Jauzac et al. 2012). None the less, these analyses remain rare because the ∼3 arcmin × 3 arcmin field of view of *HST*'s Advanced Camera for Surveys is smaller than a typical cluster's angular size. Furthermore, both of *HST*'s contiguous surveys (GOODS and COSMOS) unluckily sampled regions of the Universe that are underdense at the $z = 0.2$–0.4 redshifts where lensing is most sensitive (Heymans et al. 2005; Massey et al. 2007a; Krolewski et al. 2018), so happen to contain few lensing clusters (Guzzo et al. 2007; Massey et al. 2007b). Until recently, only around one cluster, MS 0451−03, having a dedicated wide-field mosaic of contiguous *HST* imaging had been obtained (Moran et al. 2007).

There will soon be wide-field, space-resolution imaging taken around six more clusters through the *HST*/BUFFALO survey (Steinhardt et al. 2020), 200 more clusters from the balloon-borne telescope *SuperBIT* (Romualdez et al. 2016; Romualdez et al. 2018), and 10 000 from *Euclid* (Laureijs et al. 2011). In the next decade, 40 000 clusters will be observed to even greater depth by *Nancy Grace Roman Space Telescope* (Spergel et al. 2013).

The intent of this work is to prepare for future observations, much as Van Waerbeke et al. (2013) calibrated mass mapping methods for the current generation of wide-field ground-based lensing surveys. We use mock space-based weak-lensing data to develop and quantify the performance of two different methods to map dark matter around galaxy clusters, to measure deviations from sphericity, and to search for filaments connecting it with the cosmic web. Where we must make decisions about general properties (e.g. distance, mass) of clusters that we simulate, we shall use MS 0451−03 as a template, so our predictions can be immediately tested on real observations (see our companion paper, Tam et al. 2020).

This paper is organized as follows. We summarize background theory in Section 2, and introduce the simulated data in Section 3. In the context of various scientific motivations, we describe weak-lensing mass mapping and analysis techniques in Section 4. We quantify their results in Section 5, and conclude in Section 6. Throughout the paper, we define angular diameter distances assuming a background cosmology with $\Omega_m = 0.287$, $\Omega_\Lambda = 0.713$, and $h = H_0/100 \,\mathrm{km\,s^{-1}\,Mpc^{-1}} = 0.693$ (*WMAP* 9-yr cosmology; Hinshaw et al. 2013). All magnitudes are quoted in the AB system.

2 WEAK GRAVITATIONAL LENSING THEORY

2.1 Coherent deflection of light rays

Gravitational lensing is the deflection of light rays from a distant source, by massive objects along our line of sight. The apparent shape of the source becomes distorted when a bundle of light rays from it are coherently distorted. Because cosmological distances are so large, the 3D distribution of intervening mass can be conveniently represented (through the 'thin lens' approximation) as a 2D surface density, $\Sigma(\mathbf{R})$, where $\mathbf{R} = (x, y)$ is the 2D angular position in the plane of the sky. A similar projection can be applied to obtain a 2D effective gravitational potential $\varphi(\mathbf{R})$. The angle through which

light rays are deflected corresponds to spatial derivatives in the gravitational potential.

In the weak-lensing regime, where deflection angles are small, the image distortions can be split into two dominant components. The first is an isotropic magnification, by a factor proportional to the projected density and known as 'convergence':

$$\kappa(\mathbf{R}) = \frac{\Sigma(\mathbf{R})}{\Sigma_c}, \tag{1}$$

where the 'critical density'

$$\Sigma_c = \frac{c^2}{4\pi G} \frac{D_s}{D_l D_{ls}} = \frac{c^2}{4\pi G D_l} \beta^{-1}(z_l, z_s) \tag{2}$$

depends upon the angular diameter distances from the observer to the lens, D_l, from the observer to the source, D_s, and from the lens to the source, D_{ls}. The lensing sensitivity function, $\beta(z_l, z_s) = D_{ls}/D_s$, describes the lensing strength as a function of the lens and source redshifts (z_l, z_s). For a foreground galaxy with $z_s < z_l$, $\beta(z_l, z_s) = 0$. The second component of the distortion is a shear

$$\boldsymbol{\gamma} = \gamma_1 + i\gamma_2 = |\boldsymbol{\gamma}|e^{2i\phi}, \tag{3}$$

where the real component, γ_1, represents elongation along the x direction, and the complex component, γ_2, represents elongation at $45°$.

An observable quantity, 'reduced shear'

$$\boldsymbol{g} \equiv \frac{\boldsymbol{\gamma}}{1 - \kappa} \tag{4}$$

can be measured from the apparent shapes of galaxies. In the weak-lensing regime, it is typically true that $\kappa \ll 1$; hence, $\boldsymbol{g} \approx \boldsymbol{\gamma}$. For more information, see e.g. Bartelmann & Maturi (2017).

2.2 Analytic mass distributions

In several places throughout this paper, we will approximate a mass distribution using one of two parametric models. The models are usually described in circularly symmetric form, $\Sigma(|\mathbf{R}|)$ or $\varphi(|\mathbf{R}|)$, but can be made elliptical by a coordinate transformation

$$|\mathbf{R}'|^2 = q(x^2 \cos^2 \phi + y^2 \sin^2 \phi) + (y^2 \cos^2 \phi - x^2 \sin^2 \phi)/q \tag{5}$$

(Kassiola & Kovner 1993; Oguri et al. 2010) that maps a circle to an ellipse with axial ratio $0 < q \leq 1$ and orientation ϕ. Except where mentioned explicitly, we apply this transformation to the projected mass distribution. Applying it instead to the gravitational potential yields different results, and no simple mapping exists between them.

2.2.1 tPIEMD profile

Massive elliptical galaxies are empirically observed to have an approximately isothermal density distribution ($\rho \propto r^{-2}$), and total mass proportional to the velocity distribution of their stars, σ. This would have an inconvenient mathematical singularity at the centre, which is removed in the truncated pseudo-isothermal elliptical mass distribution (tPIEMD; Kassiola & Kovner 1993; Limousin, Kneib & Natarajan 2005; Elíasdóttir et al. 2007)

$$\rho_{\mathrm{tPIEMD}} = \frac{\rho_0}{(1 + r^2/r_c^2)(1 + r^2/r_t^2)}. \tag{6}$$

This has constant density

$$\rho_0 = \frac{\sigma^2}{2\pi G} \frac{r_c + r_t}{r_c^2 r_t} \tag{7}$$

inside core radius r_c and has finite integrated mass because of the truncation at radius r_t. The projected two-dimensional mass distribution is

$$\Sigma_{\text{tPIEMD}}(R) = \frac{\sigma^2}{2G} \frac{r_t}{r_t - r_c} \left(\frac{1}{\sqrt{R^2 + r_c^2}} - \frac{1}{\sqrt{R^2 + r_t^2}} \right) . \quad (8)$$

2.2.2 NFW profile

Numerical simulations suggest that the distribution of dark matter in isolated haloes forms a Navarro–Frenk–White (NFW; Navarro, Frenk & White 1996, 1997) profile

$$\rho_{\text{NFW}} = \frac{\rho_s}{(r/r_s)(1 + (r/r_s))^2}, \quad (9)$$

where ρ_s and r_s are a characteristic density and radius. For any given cosmology and cluster redshift, this model can also be parametrized in terms of a concentration $c_{200} \equiv r_{200}/r_s$, where r_{200} is the 3D radius within which the mean enclosed density is equal to 200 times the critical density ρ_c of the Universe, and halo mass $M_{200} \equiv (4\pi/3)200\rho_c r_{200}^3$. The projected two-dimensional mass distribution (Bartelmann 1996) is

$$\Sigma_{\text{NFW}}(R) = 2\rho_s r_s F(x), \quad (10)$$

where $x = R/r_s$ and

$$F(x) = \begin{cases} \frac{1}{x^2-1} \left(1 - \frac{2}{\sqrt{x^2-1}} \arctan\sqrt{\frac{x-1}{x+1}} \right) & \text{if } x > 1, \\ \frac{1}{3} & \text{if } x = 1, \\ \frac{1}{x^2-1} \left(1 - \frac{2}{\sqrt{1-x^2}} \arctan\sqrt{\frac{1-x}{1+x}} \right) & \text{if } x < 1. \end{cases} \quad (11)$$

3 DATA

We use *N*-body particle data from the BAHAMAS suite of cosmological simulations (McCarthy et al. 2017, 2018). These were run with different background cosmologies and implementations of sub-grid galaxy formation physics, and designed to test the impact of baryonic physics on large-scale structure (LSS) tests of cosmology. For this paper, we use the version with a *WMAP* 9-yr (Hinshaw et al. 2013) cosmology, and sub-grid feedback model that is calibrated to produce a good match to the observed stellar mass function, X-ray luminosities and gas fractions of galaxy clusters. This simulation occupies a periodic cubic volume, $400\,h^{-1}$ Mpc on a side, with dark matter and (initial) baryon particle masses of 5.5×10^9 and $1.1 \times 10^9\,\text{M}_\odot$, respectively.

3.1 Distribution of mass in clusters

We extract the 10 most massive clusters from the $z = 0.5$ simulation snapshot. We first use the friends-of-friends algorithm (FOF; More et al. 2011) to identify all matter overdensities. For each FOF group, we calculate r_{200} and M_{200}, the total mass enclosed within this sphere. For the 10 most massive clusters, which have $4 \times 10^{14}\,\text{M}_\odot < M_{200} < 2 \times 10^{15}\,\text{M}_\odot$, we store the 3D distribution of dark matter, stars and gas.

To generate a 2D, pixellated convergence map, we follow the method of Robertson et al. (2019). In summary, we project the location of all simulation particles within $5\,r_{200}$ of the centre of a cluster along a line of sight (here, the simulation *z*-axis). In a 25×25 Mpc (2048×2048 pixel) map centred on the most bound particle, we use an adaptive triangular shaped cloud scheme to smooth each particle's mass over a kernel whose size depends on

the 3D distance to that particle's 32nd nearest neighbour. Resulting convergence maps are shown in Fig. 1, adopting the lens redshift $z_l = 0.55$ of galaxy cluster MS0451−03 as a concrete example, and source redshift $z_s = 0.97$ typical of *HST* observations to single-orbit depth (Leauthaud et al. 2007). The masses of the clusters are listed in Table 1.

Before proceeding further, we identify 40 filaments in the 10 projected mass maps, defined as radially extended regions with convergence $0.005 < \kappa < 0.01$, which is equivalent to a surface density of $1.7 \times 10^7 < \Sigma\,(\text{M}_\odot\,\text{kpc}^{-2}) < 3.4 \times 10^7$. These are indicated by white dashed lines in the bottom panel of Fig. 1.

3.2 Distribution of all other mass along a line of sight

In addition to the mass of the galaxy cluster itself, we also account for LSS projected by chance along the same line of sight. This is a source of noise in the projected mass of the cluster, which is then added to the mock data in Section 3.4.

To quantify the expected level of noise, we generate realizations of LSS along 1000 random lines of sight through the BAHAMAS simulation box. We then integrate the 3D mass along the line of sight, weighted by the lensing sensitivity function $\beta(z)$ with $\langle z_s \rangle = 0.97$, interpreting it as a mass distribution in a single lens plane at $z_l = 0.55$. For each realization of LSS, we calculate an effective radial density profile, $\kappa(R)$. The mean of these realizations is (unsurprisingly) consistent with zero; we also calculate the rms scatter σ_{LSS}. In concentric annuli of width $\Delta R = 25$ arcsec, these are well fitted by

$$\sigma_{\text{LSS}}(R) = \frac{A}{\sqrt{R(\text{arcsec})} + B}, \quad (12)$$

with best-fitting values for free parameters

$$A = 0.197 \pm 0.008, \quad B = 6.441 \pm 0.502. \quad (13)$$

We add this in quadrature to the statistical uncertainty on the reconstructed density profiles in Section 4.2. Note that it would also be possible to compute the full covariance matrix between LSS at different radii or in adjacent pixels of a mass map. Here, we use only the diagonal elements, but in our companion paper (Tam et al. 2020), we fit to real observations using the full covariance matrix.

3.3 Mock near-IR imaging

To generate a mock catalogue of the cluster galaxies' *K*-band magnitudes, we run SUBFIND algorithm (Springel et al. 2001) on the particle distribution from the simulations, to identify individual galaxies. We sum their stellar masses, and convert these to *K*-band luminosity based on the relation presented by Arnouts et al. (2007) for the evolution of stellar mass to light ratio, (M/L_K), with redshift for a sample of quiescent galaxies, and based on the Salpeter (1955) initial mass function. The power-law fitting function is defined as

$$\log_{10}(M/L_K) = a\,z + b, \quad (14)$$

where the mass M and luminosity L_K are in units of $\text{M}_\odot$ and $\text{L}_\odot$, respectively. The best-fitting value for parameters a and b from Arnouts et al. (2007) are

$$a = -0.18 \pm 0.04, \quad b = +0.07 \pm 0.04. \quad (15)$$

3.4 Mock weak-lensing shears

To generate mock weak-lensing observations, we convert the mass distributions into reduced shear. For the case with projected LSS,
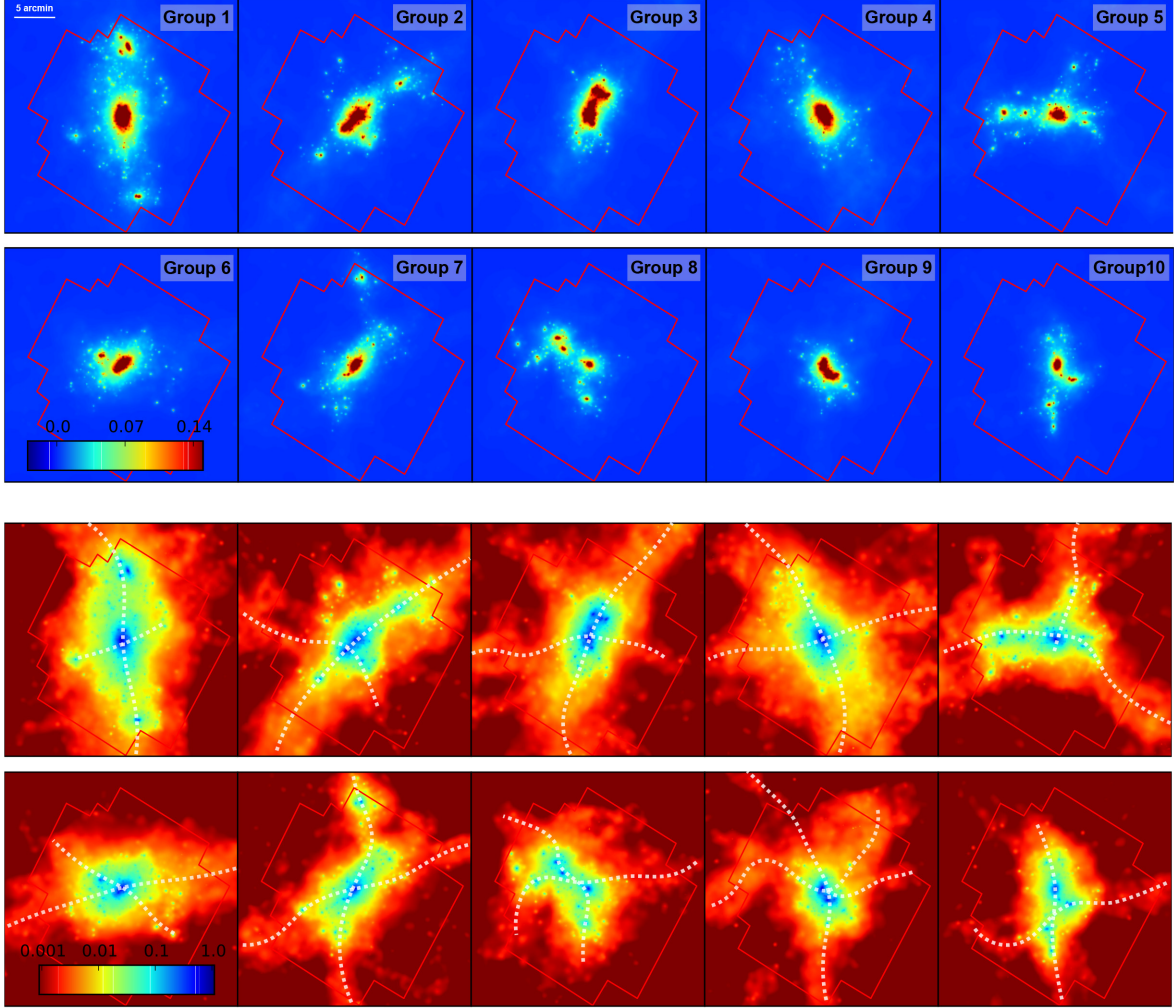
Figure 1. Noise-free maps of the total mass distribution in the 10 most massive clusters of the BAHAMAS simulations, projected along a randomly oriented line of sight. Clusters have masses M_{200} from $2 \times 10^{15}\,\mathrm{M}_\odot$ (cluster 1) to $4 \times 10^{14}\,\mathrm{M}_\odot$ (cluster 10), and are sorted in descending order of M_{FOF}, as in Table 1. Colours show the lensing convergence κ (top panel: linear scale; bottom panel: logarithmic scale). Dotted white lines show filaments identified from the noise-free, projected mass distribution, above density thresholds defined in Section 3.1. For reference, red lines indicate the field of view in which *HST* observations exist for real cluster MS 0451−03.

Table 1. Masses of the 10 most massive clusters in the BAHAMAS simulations, which we use as mock data for this study. Columns list the friends-of-friends masses M_{FOF} and overdensity mass M_{200}.

	M_{FOF} ($\times 10^{14}\,\mathrm{M}_\odot$)	M_{200} ($\times 10^{14}\,\mathrm{M}_\odot$)
Cluster 1	27.7	17.3
Cluster 2	17.9	15.0
Cluster 3	17.8	17.7
Cluster 4	16.6	14.6
Cluster 5	14.3	9.7
Cluster 6	13.3	11.0
Cluster 7	12.9	8.9
Cluster 8	11.1	4.0
Cluster 9	9.4	8.2
Cluster 10	9.3	5.7

we sum the effective convergence from the cluster (Section 3.1) and a random realization of projected LSS (Section 3.2). Since both convergence $\kappa(\boldsymbol{R})$ and shear $\boldsymbol{\gamma}(\boldsymbol{R})$ fields are linear combinations of

second derivatives of $\varphi(\boldsymbol{R})$, it is possible to directly convert between their Fourier transforms $\hat{\kappa}(\boldsymbol{k})$ and $\hat{\boldsymbol{\gamma}}(\boldsymbol{k})$

$$\hat{\gamma}_1(\boldsymbol{k}) = \frac{k_1^2 - k_2^2}{k_1^2 + k_2^2}\,\hat{\kappa}(\boldsymbol{k}), \tag{16}$$

$$\hat{\gamma}_2(\boldsymbol{k}) = \frac{2 k_1 k_2}{k_1^2 + k_2^2}\,\hat{\kappa}(\boldsymbol{k}), \tag{17}$$

where $\boldsymbol{k} = (k_1, k_2)$ is the wave vector conjugate to $\boldsymbol{R}$ (Kaiser & Squires 1993, hereafter KS93). To implement this in practice, we pixellate the fields within a 34 arcmin $\times$ 34 arcmin (2048 $\times$ 2048 pixel) grid, add zero padding to twice that linear size to mitigate boundary effects, then use discrete Fourier transforms. We finally use equation (4) to convert shear $\boldsymbol{\gamma}(\boldsymbol{R})$ into reduced shear $\boldsymbol{g}(\boldsymbol{R})$.

We generate a mock shear catalogue by randomly placing source galaxies throughout the high-resolution pixellated shear field. Mimicking typical single-orbit depth *HST* observations, we sample 50 arcmin^{-2} source galaxies. Note that we achieve a uniform density of background galaxies; in real observations, the number density of background galaxies is both clustered, and dips near the

centre of a cluster because of obscuration by, and confusion with, its member galaxies. To each shear value, we add Gaussian random noise with width $\sigma_\gamma = 0.36$, representing each galaxy's unknown intrinsic shape, plus uncertainty in shape measurement. This value matches that measured in *HST* measurements near MS 0451−03 (Tam et al. 2020), and is consistent with that measured for faint galaxies in the *HST* COSMOS field (see fig. 17 in Leauthaud et al. 2007). It is slightly larger than the intrinsic shape noise referenced elsewhere, because it also includes measurement noise.

4 METHODS

In this section, we describe several methods that have been used (or suggested) to analyse the distribution of mass in clusters. A common theme will be the suppression of noise – the two main sources of which are projected LSS, and galaxies' intrinsic shapes. In particular, sophisticated non-linear noise-suppression techniques have been developed to map the 2D distribution of mass. Even for measurements that could be obtained directly from the shear field, it may therefore be efficient to first infer (and suppress noise in) a mass map, then to measure equivalent quantities from that.

4.1 Mass mapping

We start by exploring two frequently used methods to reconstruct the distribution of lensing mass: one frequentist and the second Bayesian. Where relevant, we adopt parameters in the methods that are typically used by their protagonists.

4.1.1 Direct inversion with KS93+MRLENS

Under the weak-lensing approximation $\boldsymbol{g} = \boldsymbol{\gamma}$, the KS93 Fourier space relation (see Section 3.4) can also be used to convert $\boldsymbol{\gamma}(\boldsymbol{R})$ into

$$\hat{\kappa}(\boldsymbol{k}) = \frac{1}{2}\left(\frac{k_1^2 - k_2^2}{k_1^2 + k_2^2}\right)\hat{\gamma}_1(\boldsymbol{k}) + \frac{1}{2}\left(\frac{k_1 k_2}{k_1^2 + k_2^2}\right)\hat{\gamma}_2(\boldsymbol{k}). \tag{18}$$

This is a non-local mapping. In observations of the real Universe, any missing shear values (e.g. outside the survey boundary or behind bright stars) must be replaced via 'inpainting' (Pires et al. 2009; Raghunathan et al. 2019) to avoid suppressing the convergence signal inferred nearby. We avoid this effect by a using mock shear catalogue that is contiguous and covers a larger area (34 arcmin × 34 arcmin) than the mosaicked *HST* imaging of MS 0451−03. We bin the shear field $\boldsymbol{\gamma}(\boldsymbol{R})$ into 0.4 arcmin pixels, add zero padding out to 105 arcmin × 105 arcmin (Merten et al. 2009; Umetsu et al. 2015), and implement equation (18) using discrete Fourier transforms.

Noise was suppressed in early incarnations of KS93 by convolving the mass distribution with a larger smoothing kernel while in Fourier space. We omit this step, and instead filter the final convergence map using the Multi-Resolution method for gravitational Lensing (MRLENS; Starck, Pires & Réfrégier 2006). This decomposes an image into multiscale starlet wavelets, and applies non-linear regularization on each wavelet scale. It aims to retain statistically significant signal but suppress noise through an approach that, under the assumption of a multiscale entropy prior, optimizes the False Discovery Ratio of false detections to true detections. Starck et al. (2006) show that MRLENS outperforms Gaussian or Wiener filtering at this task, and Pires et al. (2010) demonstrate specifically that it improves the reconstruction of non-Gaussian structures like the distribution of mass in galaxy clusters.

The software implementation[1] has various free parameters: we use 10 iterations during the filtering process, and decompose the noisy 2D convergence map into six wavelet scales, starting at $j = 3$. These have size $\vartheta = 2^j$ pixels. For a starlet wavelet (equation 11 of Leonard, Pires & Starck 2012), the $j = 3$ (highest resolution) wavelet is a Mexican hat with full width at half-maximum of 0.5 arcmin. For comparison to older analyses, we also repeat the analysis after smoothing and rebinning the shear field into larger, 1 arcmin pixels.

4.1.2 Forward fitting with LENSTOOL

We also use LENSTOOL[2] (Jullo & Kneib 2009) to fit the reduced shear catalogues $\boldsymbol{g}(\boldsymbol{R})$ with a sum of analytic mass distributions. The field of view considered is the same size as the mosaicked *HST* imaging around MS 0451−03. Jullo & Kneib (2009) advocate a mass model built of three components.

(i) **Cluster-scale halo:** For clusters that produce strong gravitational lensing, the observed positions of multiple images are typically used to pre-fit the smooth, large-scale distribution of mass (Kneib et al. 1996; Smith et al. 2005; Richard et al. 2011; Jauzac et al. 2015b). Like many clusters, our mock data do not include strong lensing, so we omit this component. Note that our performance forecasts will therefore be conservative, because this information efficiently captures the broad features of a mass distribution in only a few parameters, and removes degeneracies between the remaining parameters that we shall fit (Jauzac et al. 2015a).

(ii) **Cluster member galaxies:** We model the total mass of each galaxy in the cluster as a tPIEMD (equation 8). Following Jauzac et al. (2012), their core radii, truncation radii, and velocity dispersions are scaled using empirical relations

$$r_c = r_c^*\left(\frac{L}{L^*}\right)^{\frac{1}{2}}, r_t = r_t^*\left(\frac{L}{L^*}\right)^{\frac{1}{2}}, \sigma = \sigma^*\left(\frac{L}{L^*}\right)^{\frac{1}{4}}, \tag{19}$$

where $r_c = 0.15$ kpc, $r_t = 58$ kpc and $\sigma^* = 163.10$ km ms^{-1} for a typical galaxy with *K*-band magnitude $m^* = 18.699$ at $z = 0.55$. These scaling relations describe early-type cluster galaxies (Wuyts et al. 2004), and assume a constant mass-to-light ratio for all cluster members.

(iii) **Multiscale, free-form grid:** We add a free-form (pixellated) mass distribution with spatially varying resolution that is adapted to the cluster's light distribution. Following Jullo & Kneib (2009, fig. 1), we initialize a grid of points by drawing a large hexagon over the entire field of view, split into six equilateral triangles with side length = 1152 arcsec. If a single pixel inside any of these triangles exceeds a predefined light-surface-density threshold, we split that triangle into four smaller triangles. This refinement continues for six levels of recursion, until the brightest parts of the cluster are covered by the highest resolution grid with $r_c = 18$ arcsec. We extend this grid into the cluster centre, which is inevitably modelled at the highest resolution. At the centre of every triangle, we place a circular ($q = 1$) tPIEMD (equation 8), with core radius r_c set to the side length of the triangle, truncation radius $r_t = 3r_c$, and velocity

---

[1] We implement MRLENS using the 2017 June 26 version of software available at https://www.cosmostat.org/software/mrlens. Note that a 3D extension of this method has also been developed, known as GLIMPSE (Leonard, Lanusse & Starck 2015).

[2] We implement LENSTOOL using version 7.1 of the software available at https://projets.lam.fr/projects/Lenstool/wiki.

dispersion that is free to vary. This process represents a prior that light-traces-where-mass-is, rather than explicitly light-traces-mass.

We optimize free parameters in this model using the MASSINF Markov chain Monte Carlo algorithm. The parameter space is highly dimensional, so to optimize the multiscale grid, we adopt the Gibbs approach (Jullo et al. 2007), whereby the most discrepant masses are adjusted during each step of the Markov Chain and as a prior, the initial number of RBFs to explore is set to be 2 per cent (Jauzac et al. 2012; Jullo et al. 2014). We apply a prior that the masses are all positive. This need not necessarily be true, since we are really fitting departures from the mean density of the Universe; for example, the convergence of the LSS is consistent with fluctuations around zero (Section 3.2). However, the prior is frequently used, and reasonable near a galaxy cluster. We then finally compute the marginalized mean convergence, and its 68 per cent confidence limits.

4.2 Radial density profiles

Most analyses of galaxy clusters involve fitting models of an azimuthally averaged density profile. Measuring density profiles is a key test of cosmological structure formation (e.g. the 'splashback' feature reveals a characteristic build-up of accreted mass, pausing at first apocentre after first core passage Diemer & Kravtsov 2014) and the nature of dark matter (Newman et al. 2013; Newman, Ellis & Treu 2015; Robertson et al. 2019). Because almost all clusters have irregular features, and approximately half are significantly unrelaxed (Smith et al. 2010), it is necessary to statistically combine the profiles of many clusters. This can be achieved by rescaling and averaging their density profiles in radial bins, or by fitting parametric models with radial (or elliptical) symmetry, then averaging the best-fitting parameters.

We calculate the radial density profiles of each simulated cluster by azimuthally averaging the reconstructed density maps within linearly spaced annuli of fixed width $\Delta R = 25$ arcsec. For LENSTOOL reconstructions, we quote the statistical uncertainty in each annulus, σ_{stat}, determined during the MCMC sampling. When the signal from projected LSS is included, we add σ_{LSS}, as detailed in Section 3.2, such that the total uncertainty error on the density profile, $\sigma_{tot}^2 = \sigma_{stat}^2 + \sigma_{LSS}^2$.

4.3 Halo shapes

On large scales, the accretion of matter from the surrounding large-scale environment plays a key role in determining the shape and orientation of cluster dark matter haloes (Shaw et al. 2006). Haloes are not necessarily self-similar (concentric ellipsoids with the same orientation and ellipticity; Suto et al. 2016), but align with the infall direction of subhaloes and surrounding filaments at large radii. Thus, the shape of galaxy clusters is a fundamental probe of the history of its mass accretion. Numerical simulations with collisionless dark matter predict cluster haloes to be triaxial (Warren et al. 1992; Jing & Suto 2002). Allowing DM particles to self-interact isotropizes the orbits of dark matter particles, and makes the inner mass distribution more spherical. For a cross-section of $1\,cm^2\,g^{-1}$, the median minor-to-major axial ratio 100 kpc from the halo centre is $\sim$0.8, compared with $\sim$0.5 with CDM (Robertson et al. 2019).

We fit an elliptical NFW mass distribution (equation 10) to the 2D convergence maps reconstructed from KS93+MRLENS or LENSTOOL, with no noise, with shape noise, with LSS noise or both.

The fit[3] minimize the sum of the squared difference between the reconstructed surface mass density of each BAHAMAS simulated cluster and an elliptical NFW model, within a circle of radius R_{ap}. We then vary R_{ap}, to investigate changes between the cluster's inner and outer haloes. During the fits, we fix the centre of the NFW (to the location of the most bound particle) because it is degenerate with axial ratio. We adopt flat priors on other free parameters: $0.1 \leq M_{200}\,(10^{15}\,M_{\odot}) \leq 5$, $0.1 \leq c_{200} \leq 8$, $0 \leq \phi \leq 180$, and $0.1 \leq q \leq 0.9$, and neglect covariance between adjacent pixels. The uncertainties of q in this test can be underestimated. However, it match those in observational data, as we add only one, fixed realization of LSS along the line of sight associated with each cluster.

4.4 Searches for filaments

Dark matter and gas are accreted on to a cluster mainly through filaments that connect it to the 'cosmic web'. Filaments are key transition regions in the evolution of galaxy morphology (Pandey & Bharadwaj 2006; Einasto et al. 2007; Nuza et al. 2014; Kuutma, Tamm & Tempel 2017; Liu et al. 2019; Martizzi et al. 2020) and star formation (Crain et al. 2009; White, Cohn & Smit 2010; Alpaslan et al. 2015, 2016; Yuan et al. 2019).

Filaments are much lower density environments than a cluster, so appear in gravitational lensing observations with correspondingly lower signal-to-noise. While it is possible to search for filaments directly in shear data (Dietrich et al. 2005; Dietrich et al. 2012; Jauzac et al. 2012), we explore whether it is efficient to leverage the denoising techniques developed for mass mapping, then to analyse the inferred convergence field.

4.4.1 Removing the smooth mass component

First, we subtract the smooth distribution of mass in the clusters, which would otherwise dominate the lower density contrast in the filaments.

We fit mock reduced shear data (with or without LSS and galaxy shape noise), using an elliptical NFW potential. This model has six free parameters: the coordinates of the centre of mass, (x_c, y_c), the ellipticity, $e = (1 - q^2)/(1 + q^2)$ where q is the axial ratio, the position angle, ϕ, the scale radius, r_s, and the concentration, c. We set flat priors on x_c and y_c within a 15 arcsec × 15 arcsec box centred on the most bound particle, and flat priors on $e \in$ [0.05, 0.7], $\phi \in$ [0, 180], $r_s \in$ [50, 1000] kpc, and $c \in$ [0.5, 10]. Note that we introduce ellipticity to this model via a coordinate transformation to the gravitational potential (rather than the mass, as in Section 2.2) because code to achieve this already exists within LENSTOOL.[4] The smooth distribution of mass in most simulated clusters is well approximated by a single potential. However, we use two to fit bimodal clusters 1, 2, and 9, and three for cluster 3.

We then subtract the best-fitting smooth haloes from the convergence maps. Since the mass distribution of simulated clusters cannot

---

[3]We use the SCIPY.MINIMIZE implementation of the L-BFGS-B algorithm (Byrd et al. 1995), available at https://docs.scipy.org/doc/scipy/reference/g enerated/scipy.optimize.minimize.html.

[4]An elliptical gravitational potential produces a 'boxy' mass distribution if $e > 0.6$. However, for the low values of ellipticity that we obtain, the maximum distance δR between a projected density contour and a true ellipse is $\delta R/R < 10$ per cent (see fig. 6 in Golse & Kneib 2002).
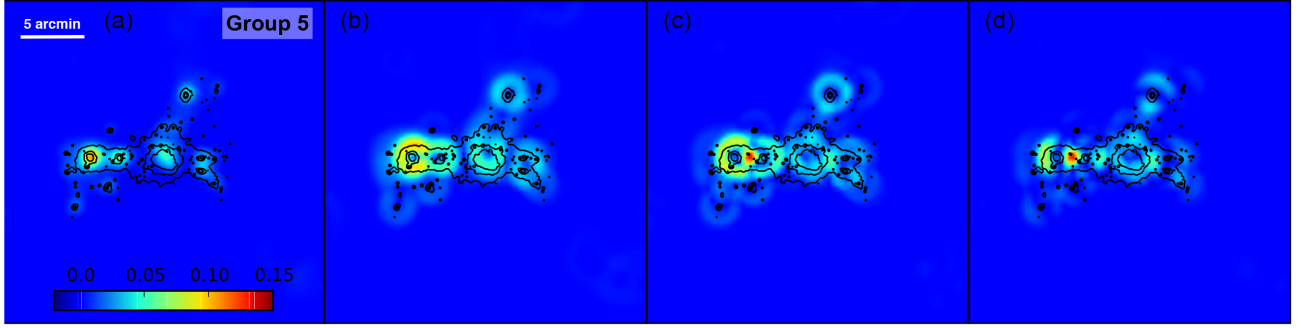
Figure 2. An example of aperture multipole moments of various orders, which pick out different features of the noise-free mass distribution of one simulated cluster (cluster 5, which happens to have several features in the plane of the sky). Moments are calculated after subtracting the large-scale smooth mass distribution. From left to right, panels show: (a) monopole, (b) dipole, (c) quadrupole moments, and (d) the radial component of the quadrupole moment. For reference, black contours show the true mass distribution.

be perfectly described by elliptical NFW potentials, small residuals are left near the cluster centre. Such residuals do not impact searches for filaments at much larger radii.

4.4.2 Aperture multipole moments

Schneider & Bartelmann ([1997](#)) first suggested looking for sub-structures or filaments using multipole moments of a convergence field within circular apertures. These are

$$Q_n(\boldsymbol{R}) = \int_0^\infty |\boldsymbol{R}' - \boldsymbol{R}|^n \, e^{ni\phi} \, U_n(|\boldsymbol{R}' - \boldsymbol{R}|) \, \kappa(\boldsymbol{R}') \, \mathrm{d}^2\boldsymbol{R}' \,, \quad (20)$$

where n is the order of the multipole, (R, ϕ) are polar coordinates, and $U_n(R)$ is a radially symmetric weight function, for which Dietrich et al. ([2005](#)) suggested

$$U_n(R) = \begin{cases} 1 - \left(\frac{R}{R_{\mathrm{max},n}}\right)^2 & \text{for } R \leqslant R_{\mathrm{max},n}, \\ 0 & \text{otherwise.} \end{cases} \quad (21)$$

Equation (20) can also be expressed in terms of shear measurements, which Dietrich et al. ([2005](#)) used to detect filament candidates in close pairs of clusters. Since modern mass reconstruction methods successfully suppress noise, we attempt instead to measure multiple moments directly from the pixellated convergence field

$$Q_n(\boldsymbol{R}) = A_{\mathrm{pix}} \sum_{i=1}^{N_{\mathrm{pix}}} R_i^n \, e^{ni\phi_i} \, U_n(R_i) \, \kappa(\boldsymbol{R}_i) \,, \quad (22)$$

where N_{pix} is the total number of pixels inside the aperture and A_{pix} is an area per pixel. For $n > 0$, Q_n is complex; we shall generally take its modulus, $|Q_n|$.

Multipoles of different orders highlight different features in a mass distribution (see Fig. [2](#)). Monopole moments ($n = 0$) are the aperture mass or normalization. Dipole moments ($n = 1$) are the local gradient of a convergence field. They form ring-like structures around mass clumps. Quadrupole moments ($n = 2$) are the locally weighted curvature or Hessian of the convergence field. As Dietrich et al. ([2005](#)) explain using a toy model, linear overdensities with a lower mass on either side (i.e. filaments) have large quadrupole moments. However, regions *between* two substructures also have large quadrupole moments. To identify the former and suppress the latter, Mead, King & McCarthy ([2010](#)) suggested combining multipole moments

$$Q \equiv \alpha_0 \, Q_0 + \alpha_1 \, Q_{+}1 + \alpha_2 \, Q_2 + \cdots \quad (23)$$

where the constants, α_i, can be adjusted to boost a signal of interest. We have tried different combinations and aperture sizes, and find that a choice of

$$\alpha_0 = -\alpha_1 = 0.7 \quad \text{and} \quad \alpha_2 = 1 \,, \quad (24)$$

$$R_{\mathrm{max},0} = 1' \quad \text{and} \quad R_{\mathrm{max},1} = R_{\mathrm{max},2} = 2' \quad (25)$$

typically highlights narrow filaments (see Fig. [3](#)). The quadrupole term is sensitive to linearly extended mass distributions, and the rings that it adds around substructures are removed by the negative dipole term. The monopole term fills in the subtracted mass, and suppresses regions between two substructures but without mass.

4.4.3 Filament identification

To identify individual filaments, we search for spatially extended regions with Q above a threshold $Q_{\mathrm{threshold}}$. The normalization of coefficients in equation (24) conveniently ensures that regions inside a contour $Q_{\mathrm{threshold}}$ have mean convergence $\langle \kappa \rangle \approx Q_{\mathrm{threshold}}$ (Fig. [4](#)). We identify as possible filaments any region with $Q > Q_{\mathrm{threshold}}$ in a contiguous area or multiple peaks with total area >1.13 arcmin^2, that is aligned within $\sim 45°$ of the radial direction to the cluster centre. Applied to noise-free data and using $Q_{\mathrm{threshold}} = 0.005$, this recipe identifies 22 of the 40 filaments, all of which are real, i.e. 55 per cent *completeness* (the number identified divided by the true number) and 100 per cent *purity* (the number identified that are true divided by the number identified). The identified filaments are highlighted in magenta in Fig. [3](#).

4.4.4 Additional noise suppression strategies

Measurements of multipole moments will be more difficult in noisy data – especially for high n moments, where the diverging $|\boldsymbol{R}' - \boldsymbol{R}|^n$ term is particularly sensitive to noise in κ near the aperture boundary. We shall explore three strategies to reduce noise. First, noise can be averaged away by enlarging the aperture. However, signal is also averaged away for a filter than is not matched to the size of the feature – and filaments are relatively narrow, even around clusters at low redshift. Secondly, negative noise peaks can be eliminated by forcing $\kappa = \max\{\kappa, 0\}$. Negative convergence is physically possible, because convergence represents deviation from the mean cosmic density; but it is unlikely along the line of sight to even a low-density structure, and probably noise rather than signal. Thirdly, we could assume that all filaments extend radially away from the
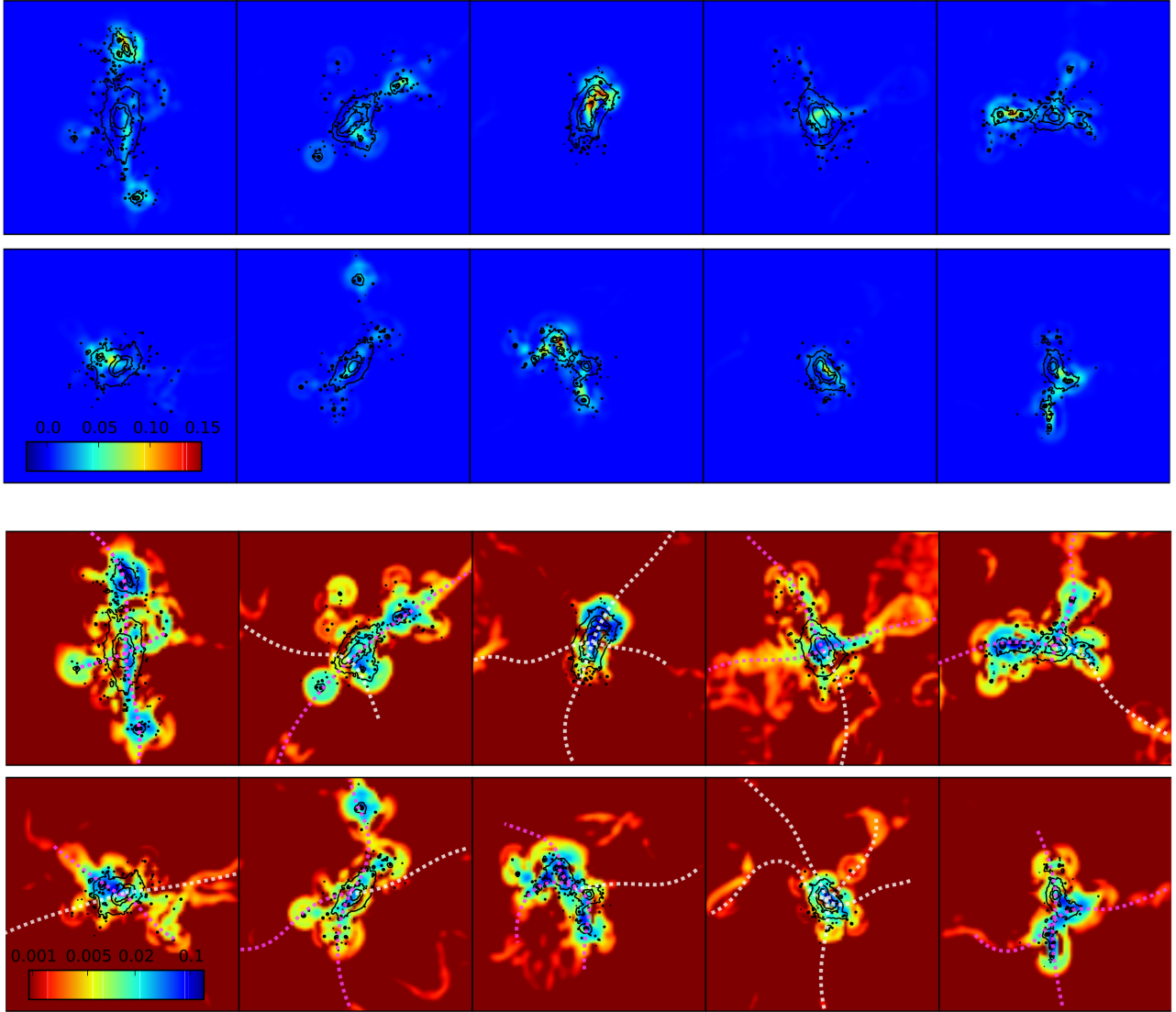
Figure 3. A combination of aperture multipole moments, Q (equations 23–25), can be used to identify filamentary features in a mass map. Colours (top panel: linear scale, bottom panel: logarithmic scale) show Q calculated from the true convergence map (without shape noise or LSS noise; black contours), after subtracting its best-fitting smooth component. Dotted lines reproduce the 40 filaments from Fig. 1. The 22 filaments successfully identified using Q and the procedure described in Section 4.4.3 are highlighted in magenta.

cluster, while noise is isotropic, and suppress quadrupole and dipole moments whose phases are tangential. We calculate

$$Q_{n,\text{projected}} = |Q_n| \cos(\phi - \theta), \quad \text{with } n = 1, 2 \quad (26)$$

where θ is an phase angle of Q_n. Fig. 2(d) shows the projected quadrupole moments in the noise-free case, as an example.

5 RESULTS AND DISCUSSION

To the 10 simulated clusters presented in Section 3, we shall now apply the analysis methods described in Section 4. We compare the reconstructed convergence maps, radial density profiles and halo shapes, to the known, true distribution of mass. We then search for observable signatures of filaments extending from the clusters. For all these analyses, we quantify the impact of the two main sources of noise in weak-lensing measurements: unrelated LSS projected by chance along the line of sight to the cluster (Section 3.2), and the intrinsic shapes of background galaxies (Section 3.4).

5.1 Mass mapping

We quantify the precision and accuracy of mass maps produced by KS93+MRLENS (Fig. 5) and LENSTOOL (Fig. 6) by comparing them to the noise-free distributions of mass, κ_{true} (which includes only the mass of the cluster, not projected LSS). We first measure deviations from this truth, $\kappa_{\text{res}} \equiv \kappa - \kappa_{\text{true}}$, to obtain the residual maps. For each map, we compute the noise level σ_κ, defined as the root mean square (rms) deviation from the mean of κ_{res}, over all pixels in a field of view equivalent in size to the *HST* observations of MS 0451-03. We then average the performance of each method over all 10 clusters (Table 2).

In observations of the real Universe, σ_κ cannot be calculated because there is no privileged knowledge of κ_{true}. For comparison with observations, we therefore also measure $\sigma_\kappa^{\text{obs}}$, the rms deviation from the mean of κ. We find values of $\sigma_\kappa^{\text{obs}}$ roughly consistent with σ_κ being added in quadrature to an irreducible component that is the rms deviation from the mean of κ_{true}, 0.022 ± 0.0007 on average (0.027 for the five highest mass clusters, or 0.017 for the five lowest).
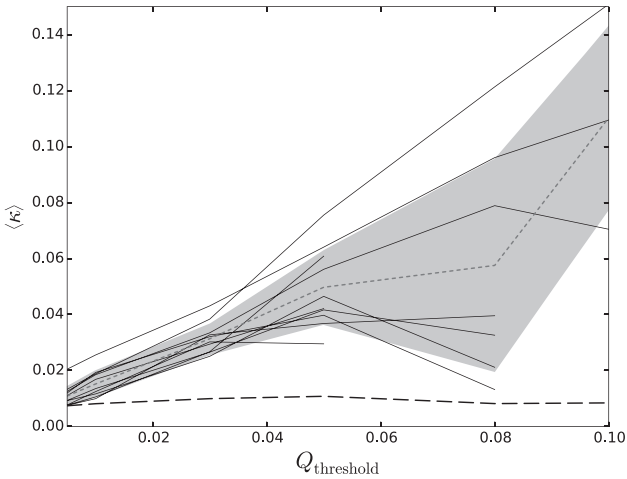
Figure 4. A combination of aperture multipole moments, Q (equations 23–25), can be used to identify features in a mass distribution with filamentary topology (see Fig. 3) and higher density than the background. Solid lines show the mean projected density $\langle \kappa \rangle$ inside a contour defined by $Q_{\text{threshold}}$, for all 10 simulated clusters. The dotted line and shaded region show their mean and standard deviation. The normalization of coefficients (24) is chosen so that $\langle \kappa \rangle = Q_{\text{threshold}}$. The lower dashed line shows the mean convergence, weighted by the number of pixels that contain $Q > Q_{\text{threshold}}$.

5.1.1 Direct inversion mass reconstruction

MRLENS suppresses galaxy shape noise by a factor 3.8 (a factor 1.5 better than smoothing with $1'$ pixels, and retaining higher spatial resolution). However, galaxy shapes still contribute more noise to the mass maps than (physically real) LSS noise. Spurious noise peaks are found in all regions of the field of view. Massive substructures with $\kappa > 0.096$ can be detected with S/N >3.

Mass reconstructions using KS93+MRLENS are statistically consistent with being unbiased. Both positive and negative noise fluctuations are produced, at all radii. The mean residual of maps with both sources of noise is $\langle \kappa_{\text{res}} \rangle = -0.0005 \pm 0.0018$, where the averaging is over 10 clusters, and the uncertainty is the standard deviation between them. The marginally negative mean may be because density is underestimated in a small region near cluster cores (see Section 5.2).

5.1.2 Forward-fitting mass reconstruction

LENSTOOL suppresses noise even further. Galaxy shape noise is an additional factor 2 lower than KS93+MRLENS (averaged across the field of view) – with the similar level as the LSS noise.

The spatial distribution of noise is non-uniform. A LENSTOOL reconstruction has more freedom in regions with a high-resolution free-form grid (Section 4.1.2), such as the cluster core and associated substructures. Spurious κ peaks appear preferentially in those regions, even when we replace the shear catalogue with one that contains only (spatially uniform) galaxy shape noise. To further investigate this effect, we split the 10 clusters into two subsamples: higher mass (clusters 1–5), and lower mass (clusters 6–10). Multiscale grids of the high-mass sample have larger high-resolution regions, resulting in noisier maps on average. Assessing the S/N of any identified peak must therefore involve bootstrap analysis at the specific region of interest. This confirms Jullo et al. (2014)'s similar assessment of the performance of LENSTOOL. For many scientific purposes, spatially varying noise is a useful

feature: the lower resolution and positive definite constraints help to suppress positive LSS noise and remove negative noise at large radii. Even filaments contain a statistically significant overdensity of galaxies (Galárraga-Espinosa et al. 2020), so the reconstruction can be given sufficient flexibility to include (rather than suppress) them.

Mass reconstructions using LENSTOOL slightly overestimate the total mass, because of its positive-definite constraint. Averaged over the field of view, the mean residual of maps with both sources of noise is $\langle \kappa_{\text{res}} \rangle = 0.0088 \pm 0.0064$ (we quote the mean of κ_{res} for 10 clusters and the standard deviation between them).

5.2 Radial density profiles

We recover the clusters' density profiles by azimuthally averaging the convergence maps (Fig. 7). The smoothing inherent to KS93+MRLENS results in an underestimation of density in the cluster core, and an overestimate just outside. This biases the inner profile slope that is often used to distinguish between cusps and cores. LENSTOOL is accurate in the cluster core, because its basis functions have a density profile that matches those of the simulated clusters. This is not affected by LENSTOOL's positive-definite constraint, because the true mass distribution is very positive near the core. In the cluster outskirts, LENSTOOL strongly suppresses galaxy shape noise, and the reconstruction is dominated by LSS noise. Because of the positive-definite constraint, this is also potentially biased. The amplitude of LSS noise varies a great deal depending on environments along the line-of-sight LSS, but we typically find artificial boosts in inferred density of up to $\sigma_{\text{LSS}} = 4 \times 10^7 \, M_\odot / \text{kpc}^2$, at large projected radii, $R > 1000 \, \text{kpc}$. This effect must be taken into account when measuring properties at large radius (e.g. M_{200}, c_{200}, splashback radius). To militate against this, measurements of galaxy redshifts will be invaluable to disentangle structures connected to the cluster from those lying in the foreground or background.

5.3 Halo shapes

Both mass reconstruction methods produce distributions that are rounder than the truth (Fig. 8). eNFW models fitted to the reconstructed mass maps (Figs 5 and 6) have a higher mean axial ratio $\langle q \rangle$ than models fitted to the true mass maps (Fig. 1). However, they successfully capture the decrease in $\langle q \rangle (R)$ at large radii that is seen in the true mass maps (reflecting a transition from dominant baryonic effects to the infall of structures along filaments; Suto et al. 2017). The orientation of most inner ($R = 650 \, \text{kpc}$) and outer ($R = 3 \, \text{Mpc}$) haloes also remain aligned within $\Delta \phi \leq 10°$, matching the true distributions (and also the simulations by Despali et al. 2017). Two exceptions to this are clusters 5 and 9, which have complex cores and $\Delta \phi = 17°$ and $\Delta \phi = 15°$. This likely indicates a transitory state during a major merger.

Using KS93+MRLENS leads to inferred values of $\langle q \rangle$ that are too high by about 6 per cent. The level of bias is not significantly influenced by either source of noise in the shear catalogue (although adding noise increases scatter in individual measurements of q as expected). It is likely due to the isotropic blurring associated with pixellization and MRLENS filtering.

Using LENSTOOL leads to inferred values of $\langle q \rangle$ that are too high by 10 per cent in the cluster core and 15 per cent in the outskirts. The bias appears to be caused by two effects:
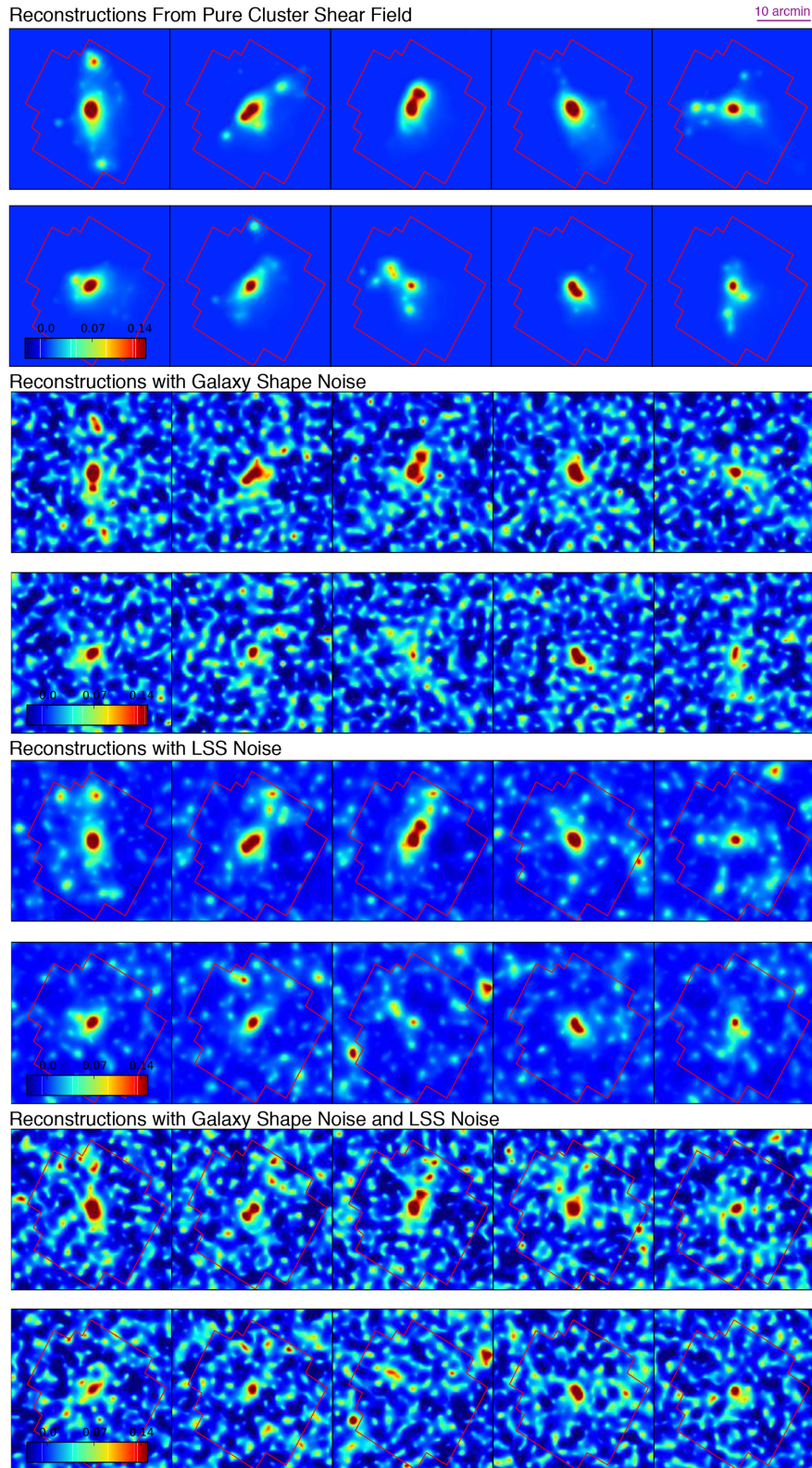
Reconstructions From Pure Cluster Shear Field

Reconstructions with Galaxy Shape Noise

Reconstructions with LSS Noise

Reconstructions with Galaxy Shape Noise and LSS Noise

Figure 5. Projected mass maps of the 10 simulated clusters reconstructed using the KS93+MRLENS direct inversion method, including different components of noise. *Top panels:* reconstruction with no noise. *Second panels:* including only shape noise from 50 background galaxies per square arcminute. *Third panels:* including only projected LSS. *Bottom panels:* including both sources of noise simultaneously. Colour scales are identical for all panels. For reference, red lines indicate the field of view of the largest *HST* mosaic obtained around a massive galaxy cluster, MS 0451−03.

Reconstructions From Pure Cluster Shear Field

Reconstructions with Galaxy Shape Noise

Reconstructions with LSS Noise

Reconstructions with Galaxy Shape Noise and LSS Noise
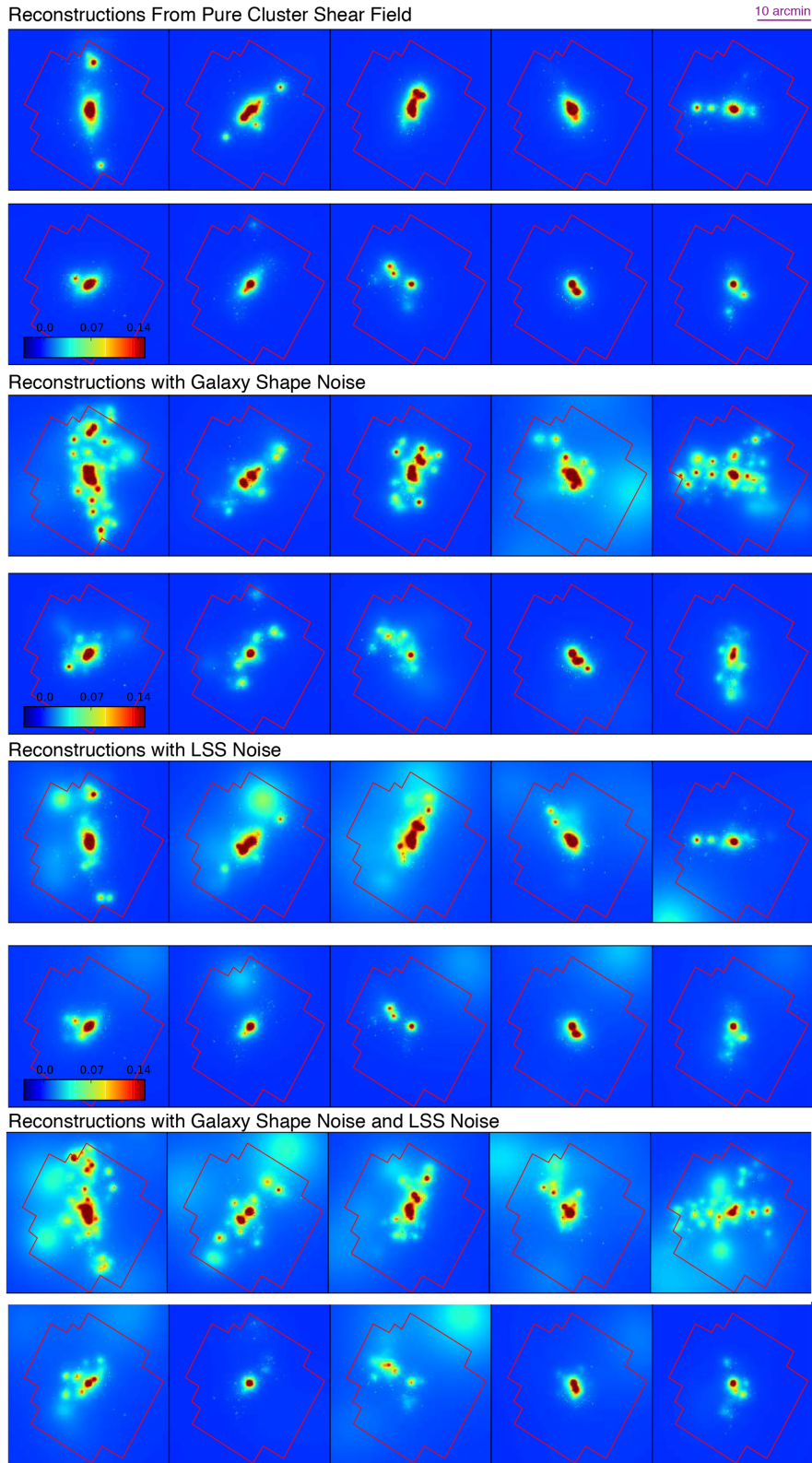
Figure 6. Same as Fig. 5, but reconstructed using LENSTOOL.

(i) The mass distribution is built from components that are all individually spherical. If the dominant halo in the cluster core is anomalously spherical (see clusters 4, 5, 8, or 10 in Fig. 9), it can bias the apparent axial ratio of the mass inside a circle by up to 10 per cent, almost regardless of the size R_{ap} of that circle. Substructures far from the centre of the cluster look surprisingly uniform, but this does not affect measurements of the overall shape.

Table 2. Noise level in mass maps created using different methods, measured as the standard deviation of all pixels inside a field of view equivalent to *HST* observations of MS 0451−03. Central values and uncertainties show the mean and standard deviation between clusters. The first three columns show deviations from the true, noise-free mass map; the second three columns show deviations from zero – which can be compared to observations of the real Universe. The 2nd, 3rd, 5th, and 6th columns refer to analyses in which the shear catalogues contain only certain sources of noise, so their relative effect can be assessed. The first two rows quantify the performance of KS93 direct inversion, with noise suppressed only via convolution with a top hat window function. The middle rows suppress noise using MRLENS. The bottom rows use LENSTOOL.

	σ_κ			$\sigma_\kappa^{\mathrm{obs}}$		
	Full mock	Shape noise only	LSS noise only	Full mock	Shape noise only	LSS noise only
KS93 (pixel scale 0.4 arcmin)	0.088 ± 0.001	0.091 ± 0.001	0.017 ± 0.002	0.090 ± 0.002	0.092 ± 0.001	0.027 ± 0.006
KS93 (pixel scale 1 arcmin)	0.037 ± 0.001	0.037 ± 0.001	0.013 ± 0.002	0.042 ± 0.003	0.039 ± 0.002	0.024 ± 0.006
KS93+MRLENS	0.026 ± 0.001	0.024 ± 0.001	0.014 ± 0.002	0.032 ± 0.004	0.028 ± 0.002	0.024 ± 0.006
High-mass clusters	0.026 ± 0.001	0.024 ± 0.001	0.016 ± 0.001	0.035 ± 0.004	0.030 ± 0.002	0.029 ± 0.005
Low-mass clusters	0.026 ± 0.002	0.024 ± 0.001	0.012 ± 0.001	0.029 ± 0.003	0.026 ± 0.001	0.019 ± 0.003
LENSTOOL	0.015 ± 0.004	0.012 ± 0.003	0.013 ± 0.004	0.023 ± 0.007	0.022 ± 0.007	0.024 ± 0.008
High-mass clusters	0.018 ± 0.002	0.014 ± 0.002	0.016 ± 0.003	0.031 ± 0.005	0.030 ± 0.005	0.030 ± 0.008
Low-mass clusters	0.012 ± 0.002	0.010 ± 0.002	0.010 ± 0.001	0.018 ± 0.003	0.018 ± 0.003	0.019 ± 0.004

(ii) The mass distribution is constrained to be positive definite. In the absence of noise, this has no effect. If we add galaxy shape noise, it is also relevant that the reconstructed mass distribution is higher resolution (has more freedom) along its major axis. The positive-definite bias in noise artefacts then exaggerates the major axis, reducing $\langle q \rangle$ by ~ 5 per cent. If we add LSS noise, $\langle q \rangle$ increases by 8 per cent because there is a larger area at close to zero convergence along the minor axis.

It is possible to mitigate the first effect by masking the cluster core. We successfully recover the true axial ratio when fitting an eNFW using to *noise-free* data inside an annulus 35 arcsec $< R < R_{\mathrm{ap}}$ (instead of a circle of radius R_{ap}). Fitting inside annuli also decorrelates measurements of $\langle q \rangle$ at different radii, and steepens the apparent gradient in $\langle q \rangle(R)$. Note that the second effect still increases $\langle q \rangle$ by ~ 6 per cent in the presence of both sources of noise.

A different strategy to mitigate sphericity bias could be to pre-fit the axial ratio of central haloes, then hold them fixed while the rest of the grid is constrained. A similar two-step process happens naturally in most combined analyses of strong plus weak lensing, where strong-lensing information constrains a cluster core. This bias should therefore not affect LENSTOOL strong-lensing analyses. However, it would be difficult to characterize statistical uncertainty in such analysis, because shear data would be used twice.

5.3.1 Comparison with previous studies

Previous work by simulators to measure the shape of cluster-scale haloes split into two distinct conclusions. Hopkins, Bahcall & Bode (2005) found that 2D cluster ellipticity increases with clustercentric radius, in agreement with our results. However, they also found that the ellipticity is $\epsilon \approx 0.05z + 0.33$ for the redshift range $0 < z < 3$, which implies $q = 0.64$ at the $z = 0.55$ redshift of our simulated clusters. Similarly, Ho et al. (2006) found $q \sim 0.616$ for haloes with masses $M > 10^{14}\,\mathrm{M_\odot}$ at $z = 0.55$ assuming $\Omega_{\mathrm{m}} = 0.3$, and $\sigma_8 = 0.7$, and little dependence upon cosmological model. Both of these results are slightly rounder than our measurement of $\langle q \rangle_{\mathrm{true}} \sim 0.55 \pm 0.03$.

More recently, Despali et al. (2017) found that $M \sim 10^{15}\,\mathrm{M_\odot}\,h^{-1}$ haloes in the SBARBINE *N*-body simulations had more elliptical shapes, with $q \sim 0.55$. Suto et al. (2016) studied the probability

distribution function (PDF) of q from projected density distributions without assumptions of self-similarity. Using their PDF fit formula for M_{vir} at $z = 0.4$, we obtain $q = 0.57 \pm 0.17$. These results match ours closely, and more recent independent analyses appear to be converging. Note that the other simulations were DM-only, but Suto et al. (2017) found that non-sphericity is unaffected by baryonic physics beyond half of the virial radius, so it is reasonable to compare to our measurements.

Several observational studies of weak-lensing have attempted to measure cluster halo ellipticity. In the Sloan Digital Sky Survey (SDSS), Evans & Bridle (2009) found a mean projected axial ratio $\langle q \rangle = 0.48^{+0.14}_{-0.09}$ in the redshift range $0.1 < z < 0.3$. By directly fitting 2D shear-maps with eNFW models, Oguri et al. (2010) measured an mean projected axial ratio $\langle q \rangle = 0.54 \pm 0.04$ for a sample of 18 X-ray luminous clusters in the redshift range $0.15 < z < 0.3$. Shin et al. (2018) measured $\langle q \rangle = 0.56 \pm 0.09$ for 10 428 SDSS clusters. These results are consistent with our measurement. Intriguingly, Umetsu et al. (2018) measured the median projected axial ratio of 20 high-mass galaxy clusters in the *HST*-CLASH survey to be $\langle q \rangle = 0.67 \pm 0.07$, within a scale of $2\,\mathrm{Mpc}\,h^{-1}$. However, their measurement from the CLASH high-magnification subsample was $\langle q \rangle = 0.55 \pm 0.11$, consistent with our results. This suggests a lensing selection bias towards haloes that are more elliptical (in the plane of the sky as well as along a line of sight). In contrast, X-ray selected clusters tend to be relaxed clusters with rounder dark matter halo shapes. For clusters selected by the red sequence technique, it is more likely that they are elongated along the line of sight, causing an overdensity of red galaxies in the projected sky-plane. Since our simulated cluster sample is selected by their high mass, with each halo projected along a random line of sight, we can only give the mass-selected mean halo shape. For direct comparison with observational data, future theoretical predictions will need to take the selection function of the observed sample into effect.

Other shape measurement techniques are possible. Studies using quadrupole estimators to quantify halo shape include Adhikari, Chue & Dalal (2015), Clampitt & Jain (2016), van Uitert et al. (2017), and Shin et al. (2018). In particular, Clampitt & Jain (2016) developed a new estimator to measure the quadrupole weak-lensing signal from 70 000 SDSS Luminous Red Galaxies haloes, and found a best-fitting axial ratio $\langle q \rangle \sim 0.78$. Their analysis assumes that dark matter perfectly aligns with light, so one potential systematic in their
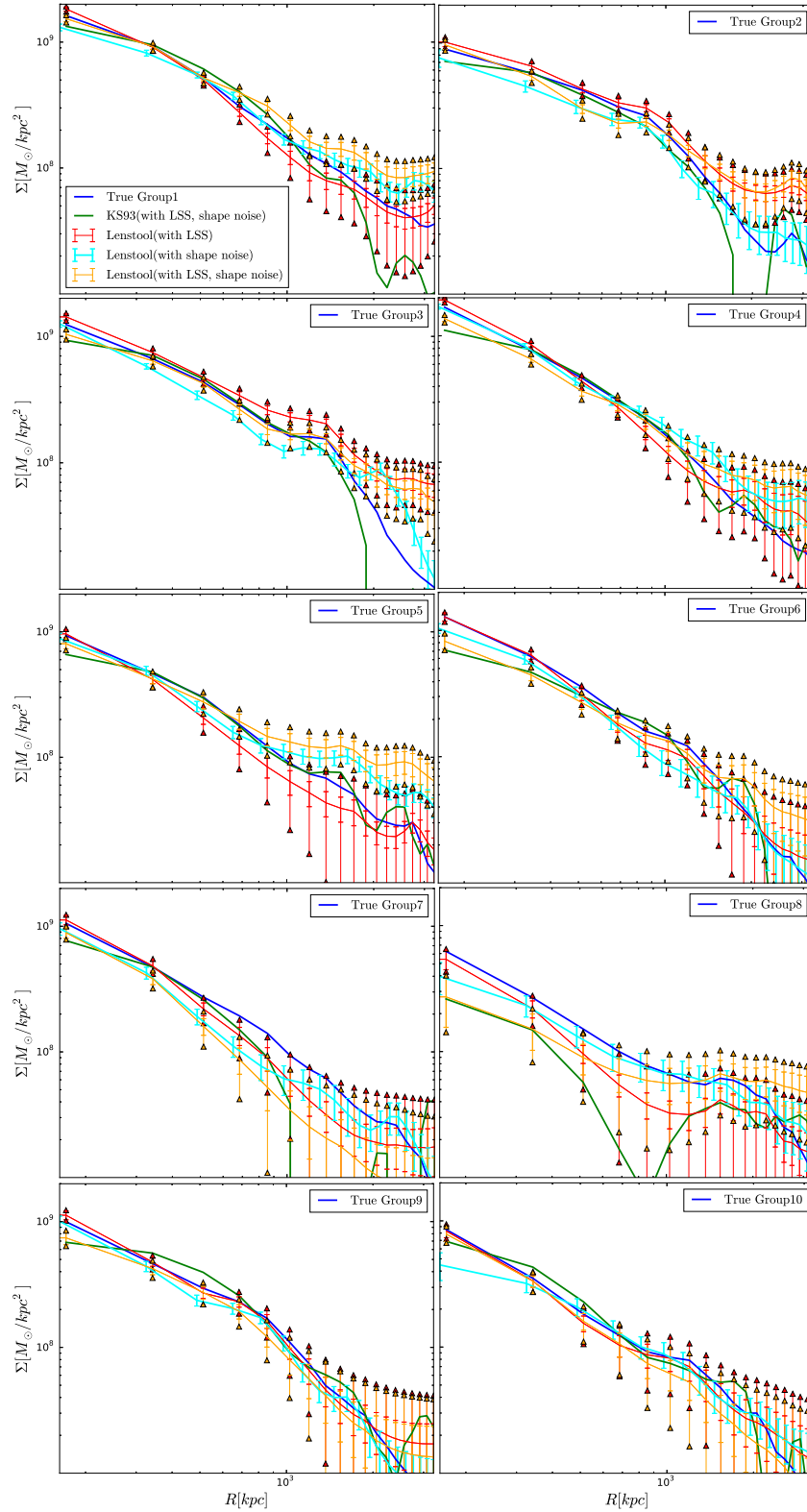
Figure 7. Surface mass density profiles for all 10 simulated clusters. Blue solid lines show the density profile calculated from the true mass distribution in Fig 1. Green solid lines are the density profiles of +MRLENS reconstructed maps after adding shapes noise and LSS. Cyan, orange, and red lines show the results recovered by LENSTOOL including shape noise, projected LSS, and both shape noise and LSS, respectively. Error bars with line caps are statistical errors from the MCMC sample. Error bars with triangle caps are total errors that are the combination of statistical errors with the estimated noise from the projected LSS (equation 12).
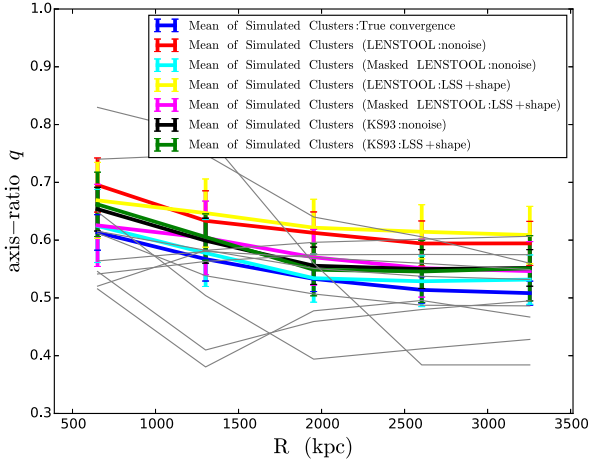
Figure 8. Best-fitting axial ratios of the mass distribution in galaxy clusters, as a function of projected, clustercentric radius *R*. Grey lines show the BAHAMAS simulated clusters, whose axial ratio profiles are measured from the true mass distribution. Blue lines show the mean and standard deviations from this set of clusters. Black (green) lines show the mean axial ratio and its scatter measured from noise-free KS93+MRLENS reconstruction (with LSS and shape noise). Red (yellow) lines show the mean results measured from noise-free LENSTOOL reconstruction (with LSS and shape noise). Cyan (magenta) lines show the axial ratio measured from the masked $R < 35$ arcsec (228 kpc) LENSTOOL reconstruction (with LSS and shape noise).

study is the possibility of light and dark matter misalignment. The determination of the orientation of each lens–source pair could become inaccurate due to this misalignment, and result in the dilution of the final stacked signal of the halo ellipticity. Indeed, applying the misalignment distribution of Okumura, Jing & Li (2009) to their measurement, they obtain $q \sim 0.6$, consistent with our results.

5.4 Searches for filaments

In the presence of galaxy shape noise and LSS noise, maps of our combination of aperture multipole moments *Q* have lower signal to noise than maps of convergence κ (Fig. 10; given the noise level, we show them only in linear scale, not logarithmic). We quantify the noise level by defining σ_Q as the standard deviation of all pixels in the final *Q* map. Despite our attempt to eliminate isolated substructures from the *Q* maps by combining different multipole moments, clusters 1, 2 and 5 contain sufficiently massive substructures to induce higher *Q* than lower density filaments. Following the methodology in Section 4.4.3, we then search for filaments as extended regions with $Q > 3\sigma_Q$ (illustrated in Fig. 10) or $Q > 4\sigma_Q$. Results for both are listed in Table 3.

In the default LENSTOOL mass reconstructions, we find $\langle\sigma_Q\rangle = 0.011$ and, with $Q_{\text{threshold}} = 3\sigma_Q$ we identify 17 of the 40 filaments (42.5 per cent completeness), plus 5 false positive detections (77.3 per cent purity). Increasing the detection threshold to $4\sigma_Q$ removes all but one false detection, but finds only 12 real filaments.

Identifying filaments in the noisier KS93+MRLENS mass reconstructions is much more difficult. To obtain useful results, we need to apply all three denoising strategies presented in Section 4.4.4. We enlarge the apertures to $R_{\text{max},0} = 2$ arcmin, $R_{\text{max, 1}} = R_{\text{max,2}} = 2.5$ arcmin; we replace negative convergence by zeros; and we project all quadrupole and dipole moments in the radial direction. In combination, these strategies reduce $\langle\sigma_Q\rangle$ from 0.11 to 0.06. Filament identification statistics after this noise suppression are listed in Table 3. At $3\sigma_Q$ detection threshold, we identify 15 of the 40 filaments (37.5 per cent completeness), but also 21 false positive detections (41.7 per cent purity).

Most of the false-positive filament detections are caused by galaxy shape noise. Repeating the KS93+MRLENS analysis with only shape noise yields a *Q* map with $\sigma_Q = 0.058$; with only LSS noise, it is $\sigma_Q = 0.033$. Because shape noise is apparently so dominant, we also investigate the effect of different survey strategies on the success of filament identification. We simulate ground-
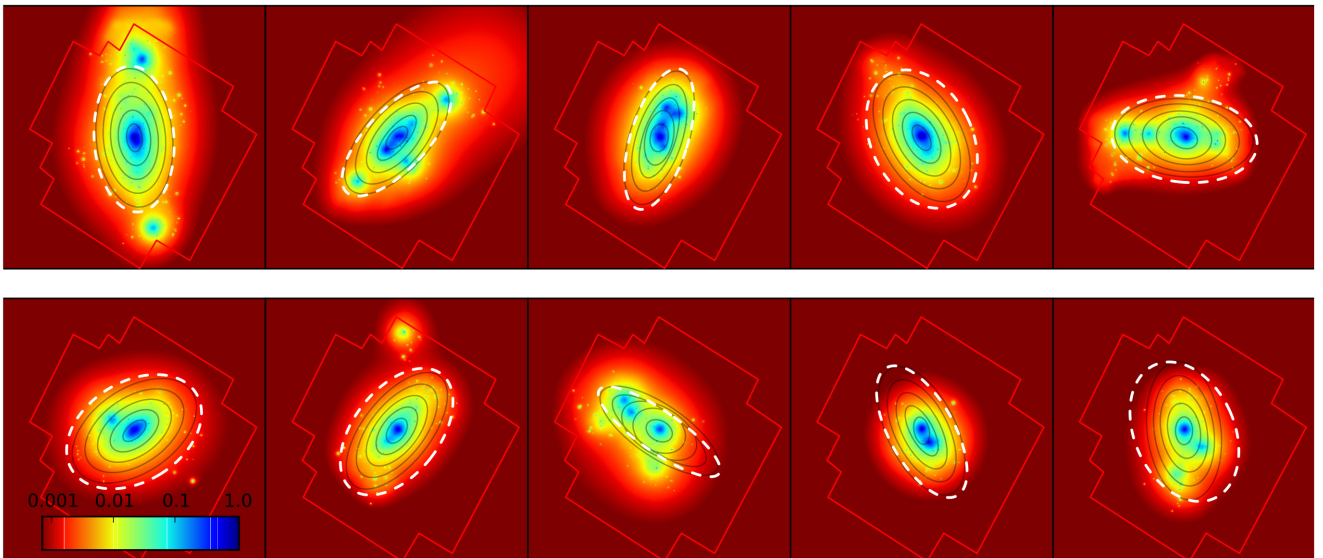

Figure 9. Elliptical eNFW models fitted to the LENSTOOL mass maps are ∼6 per cent too round, on average (see Fig. 8). Black ellipses have the same axial ratio of the true mass distribution (see Fig. 1) inside annulus $R < R_{\text{ap}}$, where different values of R_{ap} are indicated by the length of the major axis. White dashed ellipses show the axial ratio measured from masked lenstool reconstructions, inside the largest 35 arcsec $< R < R_{\text{ap}}$. The background image shows the mass distribution reconstructed by LENSTOOL, as in Fig. 6 but with a logarithmic scale to highlight one problem with the LENSTOOL method: overly circular central haloes.
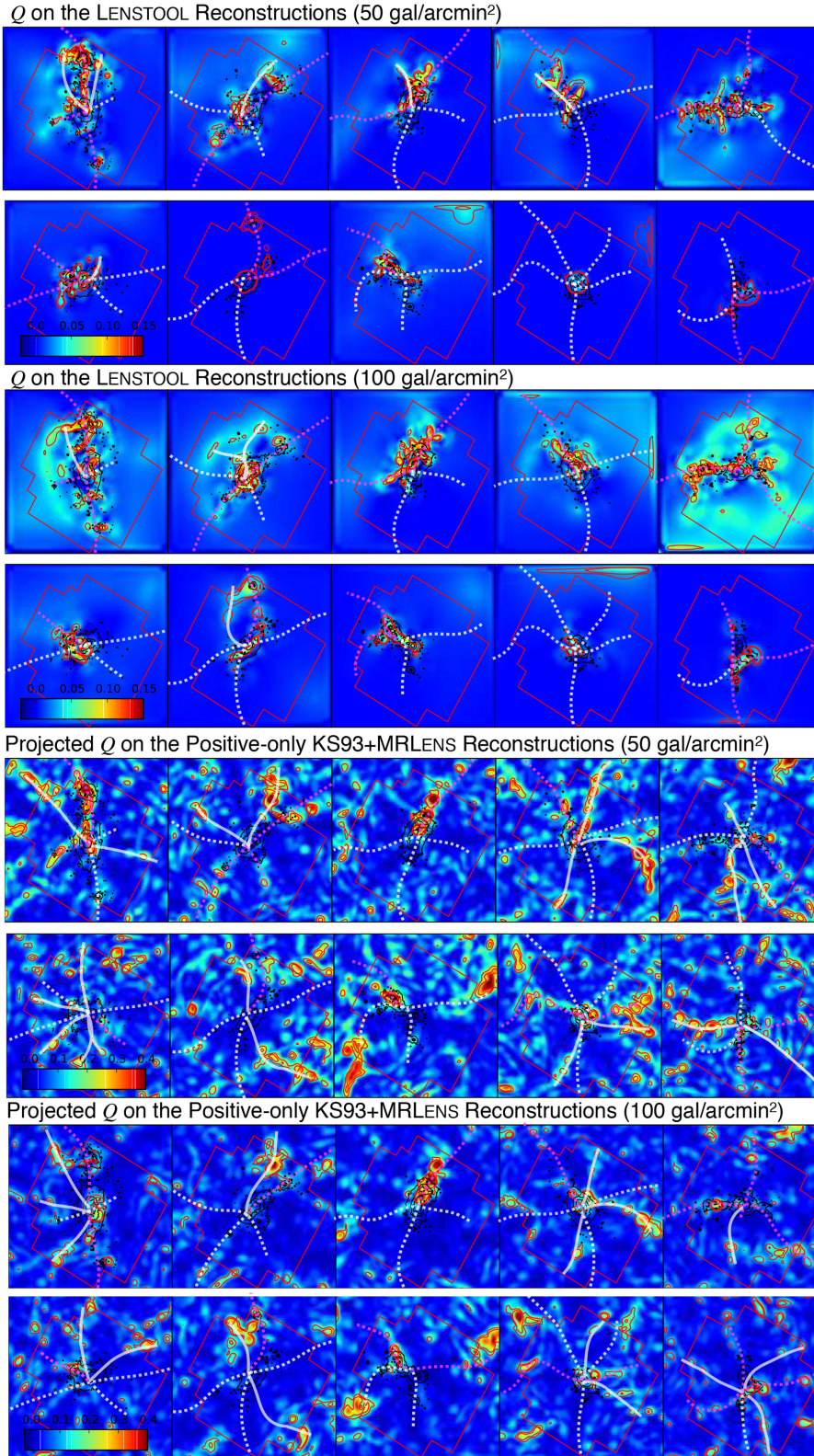
Q on the LENSTOOL Reconstructions (50 gal/arcmin²)

Q on the LENSTOOL Reconstructions (100 gal/arcmin²)

Projected Q on the Positive-only KS93+MRLENS Reconstructions (50 gal/arcmin²)

Projected Q on the Positive-only KS93+MRLENS Reconstructions (100 gal/arcmin²)

Figure 10. Results for the filament search around 10 simulated clusters. Colours show a linear combination of aperture multipole moments Q, calculated from the mass maps after subtracting their best-fitting smooth component. Dotted lines show true filaments, reproduced from Fig. 1; those identified successfully (with $Q_{threshold} = 3\sigma_Q$, see Section 4.4.3) are highlighted in magenta. Solid lines show false positive detections. The top and second panel use mass maps created by LENSTOOL (including shape noise and LSS), with 50 and 100 arcmin^{-2} source galaxies, respectively. The third and bottom panels show the phase-projected version of the filter applied to the positive-only KS93+MRLENS mass map (with a different colour scale to the top two panels). In all panels, red contours show $Q = 3\sigma_Q$ and $4\sigma_Q$, and black contours show the true mass distribution.

Table 3. Filament identification efficiency at 3σ or 4σ detection significance, from multipole aperture moments in mass maps created by KS93+MRLENS or LENSTOOL, assuming different densities of weakly lensed galaxies. Completeness indicates the fraction of the 40 real filaments (see Section 3.1) that are successfully identified. Purity indicates the fraction of the identified filaments that are real.

	Galaxy number density (arcmin^{-2})	Purity		Completeness	
		$3\sigma_Q$	$4\sigma_Q$	$3\sigma_Q$	$4\sigma_Q$
KS93+MRLENS	20	35.0 per cent	40.0 per cent	50.0 per cent	35.0 per cent
	50	41.7 per cent	44.4 per cent	37.5 per cent	30.0 per cent
	100	50.0 per cent	57.9 per cent	42.5 per cent	27.5 per cent
LENSTOOL	20	76.0 per cent	78.0 per cent	40.0 per cent	27.5 per cent
	50	77.3 per cent	92.3 per cent	42.5 per cent	30.0 per cent
	100	81.8 per cent	93.3 per cent	45.0 per cent	35.0 per cent

based observations, which typically resolve the shapes of only 20 galaxies arcmin^{-2}, and extremely deep space-based observations that resolve ∼100 galaxies arcmin^{-2} (we assume all faint galaxies have constant intrinsic shape noise, as suggested by fig. 17 of Leauthaud et al. 2007). With these catalogues, we repeat the whole analysis: including the mass reconstruction and filament search (Table 3). The low purity and high completeness of KS93+MRLENS with 20 arcmin^{-2} source galaxy is because the Q maps are filled with random noise peaks that mimic the filament signals. Some radial directions defined by the alignment of noise peaks match the true filament direction by chance and thus boost the completeness in spite of low purity. Since these maps are not informative, we show only those Q measurements using 100 arcmin^{-2} source galaxies in Fig. 10. The performance of LENSTOOL reconstructions with deep space-based data is impressive: thanks to the prior assumption of looking harder where there are galaxies, it finds 18 filaments around 10 clusters (45 per cent completeness) with 82 per cent purity. Recall that, even with noise-free data (Section 4.4.3), the maximum completeness with the multipole moment technique was 55 per cent. In general, we find that LENSTOOL is most appropriate for filament searches. Applied to future deep space-based surveys, the multipole moment technique should detect one or two filaments around most clusters.

6 CONCLUSIONS

High-precision calibration of weak-lensing mass reconstruction techniques will be essential for the next generation of space-based surveys. Understanding methods' performance in different systems (such as non-linear structures or stacked clusters), and quantifying any biases they introduce, will help identify the optimal method for each scientific analysis.

In this paper, we simulate mock observations of 10 galaxy clusters from the BAHAMAS cosmological simulation. We use their known distribution of mass $4 \times 10^{14} < M_{200}/M_\odot < 2 \times 10^{15}$ to test two mass mapping methods: (1) direct KS93 inversion from lensing shear observations to the projected mass distribution, which is then denoised using MRLENS; (2) the forward-fitting LENSTOOL technique that uses a Bayesian MCMC sampler to fit the distribution of mass in a multiscale grid. Any mass reconstruction method must interpolate the finite resolution in a shear catalogue that samples the shear field only along the lines of sight to galaxies.

We find that MRLENS is particularly efficient at suppressing noise owing to the diverse intrinsic shapes of background galaxies, while retaining signal from statistically significant structures on all scales. In a typical cluster field, it reduces total noise σ_κ from 0.088 ± 0.001 to 0.026 ± 0.001. The KS93+MRLENS method will

be appropriate for use on stacked observations of a large number of galaxy clusters. However, it has no knowledge of cluster physics, and its noise suppression via smoothing softens the inferred central density profile. At large projected radii, $R > 1$ Mpc, noise in the map of an individual cluster becomes dominated by unrelated structures at different redshifts, projected along adjacent lines of sight.

LENSTOOL incorporates physical knowledge of galaxy clusters by imposing strong priors on the distribution of mass. For example, it preserves central cusps. The method is more aggressive in denoising the reconstructed convergence field, achieving $\sigma_\kappa = 0.015 \pm 0.004$. By adjusting the grid's adaptive resolution, it is also possible to suppress the spurious signal from unrelated, isolated structures at different redshifts, once they have been identified via multiband photometry or spectroscopy. We find that this method is well suited to reconstructions of individual clusters, or measurements of low signal-to-noise quantities, such as filaments.

In its standard configuration however, we find that LENSTOOL biases a mass reconstruction at large distances from the centre of a cluster, by imposing a prior that the projected density everywhere in a field of view must be positive (relative to the mean density in the Universe). This bias will need to be managed carefully when statistical errors are reduced by averaging over a population of clusters: perhaps by reconfiguring the Bayesian optimization engine. The standard configuration of LENSTOOL also forces the mass distribution in every grid point to be spherically symmetric. In a purely weak-lensing analysis, this leads to spuriously spherical cluster cores, even when the global mass distribution is well modelled. This issue is automatically solved and irrelevant if strong gravitational lensing information is available, and used to pre-fit the axial ratio of the core. In this weak-lensing-only study, we adopt a simple solution by masking the central $R < 35$ arcsec regions of a weak-lensing-only reconstruction. This avoids modelling the central spherical core for halo shape measurement.

Based on the performance of these two methods, for an individual cluster, or measurements of highly non-linear quantities such as filament detection, LENSTOOL is well suited to applications that require as precise a reconstruction as possible. However, for high-precision analyses that stack many clusters, it would be necessary to drop LENSTOOL's positive definite constraint to reduce bias of mass overestimation. By contrast, KS93+MRLENS retains a higher level of noise, but the positive and negative fluctuations are preserved in a manner that can reduce bias in stacked measurements.

We also develop a filter to search for filaments and measure their orientation. The low density of filaments leads to low signal to noise in reconstructed maps, and they can rarely be stacked usefully. To retain their individual signal while suppressing noise, we construct a linear combination of multipole moments. We explore two further strategies: (1) filtering on the orientations (complex

phases) of higher order moments, exploiting the prior knowledge that filaments typically extend radially out of from cluster haloes and (2) replacing with the mean density of the Universe those regions inferred to have (negative) less density, which are more likely to be noise than regions inferred to have (positive) higher density. We find that it will be impossible to detect individual filaments using data from ground-based telescopes, and remains challenging with current space-based (*HST*) data. However, we find that the dominant source of noise relevant to filament detection comes from lensed galaxies' intrinsic shapes. Deeper observations with the next generation of space-based telescopes will resolve more background galaxies, and efficiently beat down this noise. Our filtering method successfully finds 45 per cent of filaments with projected density $\Sigma > 1.7 \times 10^7 \, \mathrm{M}_\odot \, \mathrm{kpc}^{-2}$ (with a false detection rate <20 per cent), when applied to mock observations at the depth of possible future surveys.

DATA AVAILABILITY

The simulation data underlying this article are available at https://www.astro.ljmu.ac.uk/~igm/BAHAMAS/.

REFERENCES

Adhikari S., Chue C. Y. R., Dalal N., 2015, J. Cosmol. Astropart. Phys., 1501, 009
Alpaslan M. et al., 2015, MNRAS, 451, 3249
Alpaslan M. et al., 2016, MNRAS, 457, 2287
Arnouts S. et al., 2007, A&A, 476, 137
Bahcall N. A., Bode P., 2003, ApJ, 588, L1
Bahcall N. A., Cen R., 1993, ApJ, 407, L49
Bartelmann M., 1996, A&A, 313, 697
Bartelmann M., Maturi M., 2017, Scholarpedia, 12, 32440
Bradac M. et al., 2006, ApJ, 652, 937
Byrd R., Lu P., Nocedal J., Zhu C., 1995, SIAM J. Sci. Comput., 16, 1190
Chiu I.-N., Umetsu K., Sereno M., Ettori S., Meneghetti M., Merten J., Sayers J., Zitrin A., 2018, ApJ, 860, 126
Clampitt J., Jain B., 2016, MNRAS, 457, 4135
Clowe D. et al., 2006, A&A, 451, 395
Crain R. A. et al., 2009, MNRAS, 399, 1773

Despali G., Giocoli C., Bonamigo M., Limousin M., Tormen G., 2017, MNRAS, 466, 181
Diemer B., Kravtsov A. V., 2014, ApJ, 789, 1
Dietrich J. P., Schneider P., Clowe D., Romano-Diaz E., Kerp J., 2005, A&A, 440, 453
Dietrich J. P., Werner N., Clowe D., Finoguenov A., Kitching T., Miller L., Simionescu A., 2012, Nature, 487, 202
Einasto M. et al., 2007, A&A, 464, 815
Elíasdóttir Á. et al., 2007, preprint (arXiv:0710.5636)
Evans A. K. D., Bridle S., 2009, ApJ, 695, 1446
Fluri J., Kacprzak T., Lucchi A., Refregier A., Amara A., Hofmann T., Schneider A., 2019, Phys. Rev. D, 100, 63514
Galárraga-Espinosa D., Aghanim N., Langer M., Gouin C., Malavasi N., 2020, preprint (arXiv:2003.09697)
Gavazzi R., Mellier Y., Fort B., Cuillandre J. C., Dantel-Fort M., 2004, A&A, 422, 407
Golse G., Kneib J. P., 2002, A&A, 390, 821
Gray M. E., Taylor A. N., Meisenheimer K., Dye S., Wolf C., Thommes E., 2002, ApJ, 568, 141
Guzzo L. et al., 2007, ApJS, 172, 254
Herbonnet R. et al., 2019, preprint (arXiv:1912.04414)
Heymans C. et al., 2005, MNRAS, 361, 160
Heymans C. et al., 2008, MNRAS, 385, 1431
Hinshaw G. et al., 2013, ApJS, 208, 19
Hoekstra H., 2013, preprint (arXiv:1312.5981)
Hopkins P. F., Bahcall N. A., Bode P., 2005, ApJ, 618, 1
Ho S., Bahcall N., Bode P., 2006, ApJ, 647, 8
Jauzac M. et al., 2012, MNRAS, 426, 3369
Jauzac M. et al., 2015a, MNRAS, 446, 4132
Jauzac M. et al., 2015b, MNRAS, 452, 1437
Jauzac M. et al., 2016, MNRAS, 463, 3876
Jee M. J., Hughes J. P., Menanteau F., Sifón C., Mandelbaum R., Barrientos L. F., Infante L., Ng K. Y., 2014, ApJ, 785, 20
Jing Y. P., Suto Y., 2002, ApJ, 574, 538
Jullo E., Kneib J.-P., 2009, MNRAS, 395, 1319
Jullo E., Kneib J.-P., Limousin M., Elíasdóttir Á., Marshall P. J., Verdugo T., 2007, New J. Phys., 9, 447
Jullo E., Pires S., Jauzac M., Kneib J.-P., 2014, MNRAS, 437, 3969
Kaiser N., Wilson G., Luppino G., Kofman L., Gioia I., Metzger M., Dahle H., 1998, preprint (arXiv:9809268)
Kaiser N., Squires G., 1993, ApJ, 404, 441
Kassiola A., Kovner I., 1993, ApJ, 417, 450
Kilbinger M., 2015, Rep. Prog. Phys., 78, 086901
Kneib J.-P., Ellis R. S., Smail I., Couch W. J., Sharples R. M., 1996, ApJ, 471, 643
Kneib J.-P., Natarajan P., 2011, A&AR, 19, 47
Krolewski A. et al., 2018, ApJ, 861, 60
Kuutma T., Tamm A., Tempel E., 2017, A&A, 600, L6
Laureijs R. et al., 2011, preprint (arXiv:1110.3193)
Leauthaud A. et al., 2007, ApJS, 172, 219
Leonard A., Lanusse F., Starck J.-L., 2015, MNRAS, 449, 1146
Leonard A., Pires S., Starck J.-L., 2012, MNRAS, 423, 3405
Limousin M., Kneib J.-P., Natarajan P., 2005, MNRAS, 356, 309
Liu C., Hao L., Wang H., Yang X., 2019, ApJ, 878, 69
Mao T.-X., Wang J., Frenk C. S., Gao L., Li R., Wang Q., Cao X., Li M., 2018, MNRAS, 478, L34
Martinet N. et al., 2016, A&A, 590, A69
Martizzi D., Vogelsberger M., Torrey P., Pillepich A., Hansen S. H., Marinacci F., Hernquist L., 2020, MNRAS, 491, 5747
Massey R., Kitching T., Richard J., 2010, Rep. Prog. Phys., 73, 086901
Massey R. et al., 2007a, ApJS, 172, 239
Massey R. et al., 2007b, Nature, 445, 286
McCarthy I. G., Bird S., Schaye J., Harnois-Deraps J., Font A. S., van Waerbeke L., 2018, MNRAS, 476, 2999
McCarthy I. G., Schaye J., Bird S., Le Brun A. M. C., 2017, MNRAS, 465, 2936
McClintock T. et al., 2019, MNRAS, 482, 1352
Mead J. M. G., King L. J., McCarthy I. G., 2010, MNRAS, 401, 2257

Medezinski E. et al., 2018, PASJ, 70, S28

Merten J., Cacciato M., Meneghetti M., Mignone C., Bartelmann M., 2009, A&A, 500, 681

Merten J. et al., 2011, MNRAS, 417, 333

Merten J. et al., 2015, ApJ, 806, 4

Miyatake H. et al., 2019, ApJ, 875, 63

Moran S. M., Ellis R. S., Treu T., Smith G. P., Rich R. M., Smail I., 2007, ApJ, 671, 1503

More S., Kravtsov A. V., Dalal N., Gottlöber S., 2011, ApJS, 195, 4

Natarajan P. et al., 2017, MNRAS, 468, 1962

Navarro J. F., Frenk C. S., White S. D. M., 1996, ApJ, 462, 563

Navarro J. F., Frenk C. S., White S. D. M., 1997, ApJ, 490, 493

Newman A. B., Ellis R. S., Treu T., 2015, ApJ, 814, 26

Newman A. B., Treu T., Ellis R. S., Sand D. J., Nipoti C., Richard J., Jullo E., 2013, ApJ, 765, 24

Nuza S. E., Kitaura F.-S., Heß S., Libeskind N. I., Müller V., 2014, MNRAS, 445, 988

Oguri M., Takada M., Okabe N., Smith G. P., 2010, MNRAS, 405, 2215

Okabe N., Smith G. P., 2016, MNRAS, 461, 3794

Okumura T., Jing Y. P., Li C., 2009, ApJ, 694, 214

Pandey B., Bharadwaj S., 2006, MNRAS, 372, 827

Pires S., Starck J. L., Amara A., Réfrégier A., Teyssier R., 2010, in Alimi J.-M., Fuözfa A., eds, AIP Conf. Ser. Vol. 1241, Cosmological Model Discrimination from Weak Lensing Data. Am. Inst. Phys., New York, p. 1118

Pires S., Starck J. L., Amara A., Teyssier R., Réfrégier A., Fadili J., 2009, MNRAS, 395, 1265

Postman M. et al., 2012, ApJS, 199, 25

Raghunathan S., Holder G. P., Bartlett J. G., Patil S., Reichardt C. L., Whitehorn N., 2019, J. Cosmol. Astropart. Phys., 2019, 037

Rehmann R. L. et al., 2019, MNRAS, 486, 77

Richard J., Kneib J.-P., Ebeling H., Stark D. P., Egami E., Fiedler A. K., 2011, MNRAS, 414, L31

Robertson A., Harvey D., Massey R., Eke V., McCarthy I. G., Jauzac M., Li B., Schaye J., 2019, MNRAS, 488, 3646

Romualdez L. J. et al., 2016, preprint (arXiv:1608.02502)

Romualdez L. J. et al., 2018, Ground-based and Airborne Instrumentation for Astronomy VII, Proc. SPIE 10702, p. 107020R

Rozo E. et al., 2010, ApJ, 708, 645

Salpeter E. E., 1955, ApJ, 121, 161

Schaye J. et al., 2015, MNRAS, 446, 521

Schneider P., Bartelmann M., 1997, MNRAS, 286, 696

Schrabback T. et al., 2018, MNRAS, 474, 2635

Schwinn J., Jauzac M., Baugh C. M., Bartelmann M., Eckert D., Harvey D., Natarajan P., Massey R., 2017, MNRAS, 467, 2913

Sereno M., Covone G., Izzo L., Ettori S., Coupon J., Lieu M., 2017, MNRAS, 472, 1946

Shaw L., Weller J., Ostriker J. P., Bode P., 2006, ApJ, 646, 815

Shin T.-h., Clampitt J., Jain B., Bernstein G., Neil A., Rozo E., Rykoff E., 2018, MNRAS, 475, 2421

Smith G. P., Kneib J.-P., Smail I., Mazzotta P., Ebeling H., Czoske O., 2005, MNRAS, 359, 417

Smith G. P. et al., 2010, MNRAS, 409, 169

Spergel D. et al., 2013, preprint (arXiv:1305.5422)

Springel V., White S. D. M., Tormen G., Kauffmann G., 2001, MNRAS, 328, 726

Springel V. et al., 2005, Nature, 435, 629

Starck J.-L., Pires S., Réfrégier A., 2006, A&A, 451, 1139

Steinhardt C., et al., 2020, ApJS, 247, 64

Suto D., Kitayama T., Nishimichi T., Sasaki S., Suto Y., 2016, PASJ, 68, 97

Suto D., Peirani S., Dubois Y., Kitayama T., Nishimichi T., Sasaki S., Suto Y., 2017, PASJ, 69, 14

Tam S.-I. et al., 2020, preprint (arXiv:2006.10156)

Treu T., Ellis R. S., 2015, Contemp. Phys., 56, 17

Umetsu K. et al., 2014, ApJ, 795, 163

Umetsu K. et al., 2015, ApJ, 806, 207

Umetsu K. et al., 2018, ApJ, 860, 104

Umetsu K. et al., 2020, ApJ, 890, 148

van Uitert E. et al., 2017, MNRAS, 467, 4131

Van Waerbeke L. et al., 2013, MNRAS, 433, 3373

von der Linden A. et al., 2014, MNRAS, 439, 2

Warren M. S., Quinn P. J., Salmon J. K., Zurek W. H., 1992, ApJ, 399, 405

Weinberg D. H., Bullock J. S., Governato F., Kuzio de Naray R., Peter A. H. G., 2015, Proc. Natl. Acad. Sci., 112, 12249

White M., Cohn J. D., Smit R., 2010, MNRAS, 408, 1818

White S. D. M., Rees M. J., 1978, MNRAS, 183, 341

Wuyts S., van Dokkum P. G., Kelson D. D., Franx M., Illingworth G. D., 2004, ApJ, 605, 677

Yuan L. et al., 2019, MNRAS, 487, 1315

This paper has been typeset from a TeX/LaTeX file prepared by the author.